# Observationally constrained regional variations of shortwave absorption by iron oxides emphasize the cooling effect of dust

Vincenzo Obiso[1], María Gonçalves Ageitos[2,3], Carlos Pérez García-Pando[2,4], Gregory L. Schuster[5], Susanne E. Bauer[1], Claudia Di Biagio[6], Paola Formenti[6], Jan P. Perlwitz[1,7], Konstantinos Tsigaridis[8,1], and Ronald L. Miller[1]

[1]NASA Goddard Institute for Space Studies, New York, NY, USA
[2]Barcelona Supercomputing Center, Barcelona, Spain
[3]Polytechnic University of Catalonia, Barcelona, Spain
[4]ICREA, Catalan Institution for Research and Advanced Studies, Barcelona, Spain
[5]NASA Langley Research Center, Hampton, VA, USA
[6]Université Paris Cité and Univ Paris Est Creteil, CNRS, LISA, F-75013 Paris, France
[7]Climate, Aerosol, and Pollution Research, LLC, Bronx, NY, USA
[8]Center for Climate Systems Research, Columbia University, New York, NY, USA

**Correspondence:** Vincenzo Obiso (obisovincenzo@gmail.com)

**Abstract.** The composition of soil dust aerosols derives from the mineral abundances in the parent soils that vary across dust source regions. Nonetheless, Earth System Models (ESMs) have traditionally represented mineral dust as a globally homogeneous species. The growing interest in modeling dust mineralogy, facilitated by the recognized sensitivity of the dust climate impacts to composition, has motivated state-of-the-art ESMs to incorporate the mineral speciation of dust along with

5  its effect upon the dust direct radiative effect (DRE). In this work, we enable the NASA Goddard Institute for Space Studies ModelE2.1 to calculate the shortwave (SW) DRE by accounting for the regionally varying soil mineralogy. Mineral-radiation interaction at solar wavelengths is calculated according to two alternative coupling schemes: 1) external mixing of three mineral components that are optically distinguished, one of which contains embedded iron oxides; 2) a single internal mixture of all dust minerals with a dynamic fraction of iron oxides that varies regionally and temporally. We link dust absorption to the

10  fractional mass of iron oxides based on recent chamber measurements using natural dust aerosol samples. We show that coupled mineralogy overall enhances the scattering by dust, and thus the global cooling, compared to our control run with globally uniform composition. According to the external mixing scheme, the SW DRE at the top of atmosphere (TOA) changes from $-0.25$ to $-0.30\,W \cdot m^{-2}$, corresponding to a change in the net DRE, including the longwave effect, from $-0.08$ to $-0.12\,W \cdot m^{-2}$. The cooling increase is accentuated when the internal mixing scheme is configured: SW DRE at TOA becomes $-0.34\,W \cdot$

15  $m^{-2}$ (with a net DRE of $-0.15\,W \cdot m^{-2}$). The varying composition modifies the regional distribution of single scattering albedo (SSA), whose variations in specific regions can be remarkable (above $0.03$) and significantly modify the regional DRE. Evaluation against the AErosol RObotic NETwork (AERONET) shows that explicit representation of soil mineralogy and its regional variations reduces the low bias of model dust SSA, while improving the range of variability across stations and calendar months. Despite these improvements, the moderate spatio-temporal correlation with AERONET reveals remaining

20  modeling challenges and the need for more accurate measurements of mineral fractions in soils.

## 1 Introduction

Dust aerosols are wind-blown soil particles that alter the atmospheric energy and hydrologic cycles by perturbing solar and thermal radiative fluxes (Miller et al., 2014). Estimates of the dust direct radiative effect (DRE) are still largely uncertain, mainly due to poorly constrained dust absorption (Samset et al., 2018). The single scattering albedo (SSA) indicates the frac-
25   tion of radiative energy extinguished by aerosols through scattering with respect to total extinction, due to both scattering and absorption, and therefore inversely measures the intrinsic aerosol absorptive power. The SSA is a function of the particle size distribution (PSD), complex refractive index (CRI) and shape (Hansen and Travis, 1974; Mishchenko et al., 2002). Despite substantial regional variations in soil composition (Claquin et al., 1999; Journet et al., 2014), nearly all Earth System Models (ESMs) assume a globally homogeneous composition for dust aerosols, thus attributing only to PSD the spatio-temporal vari-
30   ations of dust SSA, while neglecting the contribution of the CRI that varies according to the relative abundance of different minerals. In particular, iron oxides like hematite and goethite strongly absorb radiation at ultra-violet (UV) and visible (VIS) wavelengths (Di Biagio et al., 2019; Moosmüller et al., 2012), which largely impacts the imaginary part of the CRI (IRI). In addition to underestimating the SSA variations in space and time, this neglect of composition variations has contributed to a range of assessments of the dust DRE, as climate models usually employ dust CRIs derived from measurements in specific
35   regions that are assumed to be globally representative (Miller et al., 2006; Colarco et al., 2014). For example, two different absorption regimes for dust produced a DRE of opposite sign at the top of atmosphere (TOA) in West Africa, with consequent hydrologic and thermodynamic effects (Miller et al., 2004; Strong et al., 2015). This indeterminacy has consequences for understanding the dust effect upon the present-day climate along with past climates like the African Humid Period (Miller et al., 2014; Pausata et al., 2016). One path forward is to explicitly represent the contribution of regionally varying soil composition
40   in the calculation of dust optical properties and the DRE (Scanza et al., 2015; Li et al., 2021).

   Sokolik and Toon (1999) described an early calculation of the dust DRE based on mineral composition. They compiled the CRI for several climatically relevant minerals (such as quartz, phyllosilicates and the iron oxide hematite) and calculated the resulting CRI of a dust particle that was an amalgam of those minerals with prescribed proportions. They showed that absorption at solar wavelengths is dominated by hematite, an iron oxide that is often present in trace amounts, accreted within
45   other minerals. This conclusion was corroborated by Balkanski et al. (2007), who calculated that dust particles containing $1.5\%$ of hematite by volume in an internal mixture, including quartz and phyllosilicates, were in best agreement with AERONET retrievals. Both studies derived the CRI of the amalgam from the CRIs of individual minerals through a mixing rule. Commonly used rules range from empirical (e.g. volume-weighted mean: VM) to rigorously derived relations based on an assumed internal structure of the particle, such as for example Maxwell Garnett (MG) and Bruggeman (BG) (Markel, 2016). The use of any
50   single mixing rule is only approximate, given the limitations of validity conditions and mathematical difficulties (Markel, 2016) along with the variety and complexity of observed dust particle morphology (Scheuvens and Kandler, 2014). Moreover, estimates of hematite IRI that can be found in literature vary widely, thus indicating high structural uncertainty (Zhang et al., 2015).

However, measurements suggest that the derivation of the particle IRI in terms of its constituent minerals can be simplified in some wavelength ranges. Moosmüller et al. (2012) showed that dust SSA at two solar wavelengths decreased in proportion to the fractional mass of iron within a collection of aerosolized soil samples. Di Biagio et al. (2019, hereafter DB19) revisited this relation by aerosolizing nineteen natural soil samples collected from dust source regions worldwide, and related retrievals of dust IRI at UV, VIS and near-infrared (NIR) wavelengths to the abundance of iron oxides in the dust aerosol samples. These experimental results suggest an innovative method for calculating the particle IRI at solar wavelengths as a function of the mass fraction of iron oxides that would circumvent the need for a theoretical rule approximating the physical arrangement of minerals within a dust particle. The approach would complement the method by Scanza et al. (2015, hereafter SZ15) and Li et al. (2021), who followed Sokolik and Toon (1999) and Balkanski et al. (2007) by invoking an explicit mixing rule.

In this work, we update the NASA GISS ModelE2.1 (Kelley et al., 2020) to calculate dust optical properties in the UV-VIS band, along with the DRE in the shortwave (SW) spectral region, by accounting for the spatially and temporally varying mineral composition of dust aerosols that is calculated by the model (Perlwitz et al., 2015a). Our approach is based on the empirical relation between the fractional mass of iron oxides and the dust IRI retrieved by DB19. We implement two schemes for assigning minerals to radiatively active dust types, allowing us to test the sensitivity of our results to the mixing state of minerals, which is constrained by few measurements. We assess the effect of varying composition upon the model calculation of dust optical depth (DOD), SSA and DRE. We also evaluate the model DOD and SSA against observations and retrievals from the AErosol RObotic NETwork (AERONET; Holben et al., 1998). This evaluation is challenged by the presence of other aerosol species that are also detected by AERONET. In particular, sea salt (present mainly in coastal areas) may contribute to the coarse mode, and above all, black carbon (BC) and brown carbon (BrC) affect the absorption by the aerosol mixture even in small proportions. Hence, we filter AERONET scenes to identify hourly measurements where dust is the dominant component by applying multiple conditions based on both the size and the absorption features of different aerosol species at solar wavelengths. Our approaches aim to minimize uncertainties in the modeling of dust optical properties for mineral mixtures as well as in the comparison with AERONET dust-filtered measurements.

In Section 2, after a description of ModelE2.1 (Section 2.1), we present our methodology for coupling radiation calculations to dust mineral composition (Section 2.2); we then illustrate our filtering technique to select dusty scenes from AERONET (Section 2.3). In Section 3, we present the effect of composition variations upon model dust optical properties (DOD and SSA) and DRE (Section 3.1), and the comparison between model and AERONET (Section 3.2). Finally, in Section 4, we discuss the main sources of uncertainty in our modeling method.

## 2 Methods

### 2.1 Atmospheric Model

The NASA GISS ModelE is a modular model that can simulate many components of the Earth System and their interaction through energy and mass fluxes, including atmosphere and ocean circulation, atmospheric chemistry and aerosols (Schmidt et al., 2014; Kelley et al., 2020). The ModelE2.1 version is the first GISS contribution to the Coupled Model Intercomparison

Project Phase 6 (CMIP6) (Kelley et al., 2020; Miller et al., 2021). In this work, we use an upgraded version of ModelE2.1, including minor bug fixes and the new coupling between minerals and radiation (Section 2.2). We run global simulations with the atmospheric model (i.e. with prescribed oceans) setting a horizontal resolution of $2.0°$ latitude by $2.5°$ longitude and forty

90  vertical layers extending to $0.1\,hPa$. Interactive dust minerals are calculated using the One-Moment Aerosol (OMA) module, a mass-based scheme for externally mixed aerosols that can simulate a full set of aerosols including sulfate, nitrate, ammonium, black carbon, organic carbon, secondary organic aerosol, sea salt and dust (Bauer et al., 2020). In our experimental setup, ozone and aerosols other than dust are prescribed from simulations of the CMIP6 historical period (1850-2014) with the ModelE2.1 version of the OMA module (Bauer et al., 2020).

95  The general calculation of dust emission, transport and deposition in ModelE2.1 is described in Miller et al. (2006); individual mineral tracers were implemented by Perlwitz et al. (2015a). Mineral dust is emitted when the model wind speed exceeds a threshold that has a globally uniform minimum value of $8\,m \cdot s^{-1}$ for completely dry soils, and increases with the local soil wetness that can vary with time. Dust sources correspond to regions with sparse vegetation and easily erodible soil particles, identified by topographic depressions (Ginoux et al., 2001). In the mineral version of the dust module, the total emitted flux

100  is partitioned among the size-distributed mass fractions of individual minerals, that vary with the local properties of the parent soils but are constant in time. The mineral fractions are determined by combining the Mean Mineralogical Table (MMT) of Claquin et al. (1999), that provides normalized mineral fractions within the clay and silt size categories for a number of soil types, with the geographical distribution of soil types and soil textures, the latter giving the fractional mass in each size category. Additionally, since both the MMT and soil texture data refer to disturbed soils, that is samples in which soil aggre-

105  gates were broken due to wet-sieving techniques, we apply an algorithm based on the Brittle Fragmentation Theory (BFT; Kok, 2011) to reconstruct the dust aggregates originally emitted from soils, both for determining the (globally uniform) emitted mass fractions of total dust in the clay and silt categories, and for adjusting the mineral fractions in the silt category to account for the broken aggregates of specific minerals. Finally, we distribute the mineral fractions within the silt bins of ModelE2.1 (Table B2) and determine the emitted PSD also for diameters larger than $20\,\mu m$ (which is the upper range of validity for BFT) by using

110  dust measurements at Tinfou, Morocco (Kandler et al., 2009). We refer to Perlwitz et al. (2015a) for a detailed description of the theoretical derivation of our Aerosol Mineral Fraction (AMF) method.

ModelE2.1 transports eight minerals listed in Table 1; hematite, as prescribed by Claquin et al. (1999), is interpreted as a proxy for a broader class of iron oxides including goethite. Most iron oxides are observed as trace abundances accreted within other minerals (Formenti et al., 2008). ModelE2.1 represents these accretions as an internal mixture of iron oxides with each

115  of the remaining seven minerals (the latter referred to as 'host' minerals), creating seven additional transported dust types for a total of fifteen (Perlwitz et al., 2015a). We refer to each of the seven host minerals accreted with iron oxides (the latter contributing a fixed $5\,\%$ of the particle mass) as 'accretions'. The accretion of a small fraction of iron oxides within another mineral allows them to travel farther, as in pure form they would settle more rapidly due to their larger density (Table 1).

The fifteen particle types are emitted and transported within five size bins ranging from $0.1$ to $32\,\mu m$ in diameter (Table

120  B2). To allow a more precise representation of dust-radiation interactions at UV-VIS wavelengths, the clay bin (from $0.1$ to $2\,\mu m$ in diameter) is split into four sub-bins according to constant weights based on the emitted PSD from BFT (Perlwitz

**Table 1.** Mass densities of transported minerals ($\rho_{min}$) as prescribed in ModelE2.1 (Perlwitz et al., 2015a). For iron oxide tracers in pure crystalline form, the arithmetic mean between hematite ($5.260\,g \cdot cm^{-3}$) and goethite ($4.280\,g \cdot cm^{-3}$) is used. The density of each mineral accreted with iron oxides is calculated from the densities of the single minerals according to their fraction in the particle.

| Mineral | $\rho_{min}\,[g \cdot cm^{-3}]$ |
|---|---|
| Illite | 2.795 |
| Kaolinite | 2.630 |
| Smectite | 2.350 |
| Calcite | 2.710 |
| Quartz | 2.655 |
| Feldspar | 2.680 |
| Gypsum | 2.312 |
| Iron oxides | 4.770 |

et al., 2015a). Aerosol removal occurs through dry processes (i.e. the combined effect of gravitational settling and turbulent surface deposition) along with wet deposition. The latter is the result of below-cloud scavenging by impaction that depends upon aerosol size but is otherwise identical for all aerosol species (Koch et al., 1999). In addition, soluble aerosols are removed through nucleation of droplets within clouds. One half of dust particles are assumed to be soluble.

The global magnitude of dust emission is uncertain due to a scarcity of direct observations and the limited resolution of the model wind speed that has a non-linear influence upon emission (Cakmur et al., 2006). For this reason, we calibrate global emission by matching a worldwide array of observations (Cakmur et al., 2006). This calibration is identical for all our experiments, so that differences in mass load between the experiments are the result of a feedback of the dust DRE upon emission (e.g. Miller et al., 2004; Pérez et al., 2006; Heinold et al., 2007; Ahn et al., 2007).

## 2.2 Coupling of dust mineralogy to radiation calculations

We demonstrate the effect of spatial and temporal variations in mineral composition upon the dust optical properties (DOD, SSA) in the UV-VIS band, along with the SW DRE, by comparing two mineral experiments ('EXT' and 'INT') that account for the content of iron oxides, to a control run ('HOM') that instead prescribes globally homogeneous composition. The contrast between the EXT and INT experiments reveals the sensitivity of our results to two alternative mineral-radiation coupling schemes. For each of the three experiments, we calculate a climatology from a thirty year simulation (1991–2020), setting one year of spin-up, with greenhouse gas concentrations and prescribed atmospheric composition of the year 2000.

We calculate the CRIs used in the mineral experiments by merging the dust IRI retrievals from DB19 with the collection of CRIs of individual minerals from SZ15. DB19 measured SW scattering and absorption spectra, volume size distribution and bulk mineral composition of nineteen dust aerosol samples generated from parent soil samples and injected within a laboratory chamber. They then retrieved the CRI of the dust aerosols at seven SW wavelengths, and observed an increasing relation of the retrieved IRI to the content of iron oxides in each aerosol sample (Section 2.2.3). Due to their experimental setup, DB19

retrieved one CRI for each sample, thus implicitly representing dust particles as identical internal mixtures of all minerals, with uniform composition across sizes but varying among samples. (AERONET similarly assumes an internal mixture of
145    constituents that is identical at all sizes and for all particles in the column.) This description is more consistent with our INT coupling scheme (except for the variation in composition with size that we assume), whereas in the EXT scheme we assume that iron oxides are internally mixed with only a (varying) fraction of host minerals (Section 2.2.1).

    In Sections from 2.2.1 to 2.2.4, we describe our strategy for modeling radiatively active mineral components and calculating the corresponding CRIs. In Appendix B1, we report the CRIs used in all our experiments (Table B1) and describe in detail our
150    computation of dust optical properties in the SW spectrum, with and without accounting for varying mineral composition.

### 2.2.1    Mixing configurations for minerals

To relate mineral composition to radiation parsimoniously, we redistribute the fifteen mineral tracers to a smaller number of radiatively active aerosol components, according to two alternative coupling schemes. In our first scheme (EXT), we use the mineral combinations calculated by ModelE2.1 (Section 2.1). For each size bin, we assemble the mass of the fifteen mineral
155    tracers into three components: 1) iron oxides by themselves ('free' or 'crystalline' iron oxides), 2) the remaining seven host minerals together and 3) the seven accretions of iron oxides within each host mineral together. We then assign a different (globally uniform) CRI to each of the three mass components, by assuming a simplified optical model: the host minerals are considered as a globally uniform amalgam ('host mixture'), while the accretions as an internal mixture of the host amalgam and a fixed mass fraction of iron oxides ('static accretion'). It follows that the EXT scheme does not assume a 'pure' external
160    mixing of all minerals, instead it assumes external mixing of two internal mixtures (one of which contains embedded iron oxides) plus free iron oxides. In Figure 1, we show a schematic cartoon of the mixing state of minerals in both our coupling schemes. Because the mass fraction of iron oxides in the static accretion is fixed at $5\%$ (Section 2.1), in the EXT scheme mineral-induced variations of dust optical properties in space and time result solely from the varying proportion of the three components. The reduction of the fifteen mineral tracers to three radiative types is a simplification based on the observation
165    that iron oxides dominate dust absorption at UV-VIS wavelengths (Sokolik and Toon, 1999; Zhang et al., 2015), while the IRIs of the seven host minerals are much smaller (Scanza et al., 2015).

    In the second coupling scheme (INT), we assume that all minerals (including iron oxides) are part of a single size-resolved internal mixture. We refer to this mixture as a 'dynamic accretion', in contrast with the static accretion of our model-derived EXT scheme, because the particle composition in each bin and the associated CRI vary locally according to the constantly
170    changing proportion of iron oxides at any grid box and time step (Figure 1). While our model explicitly calculates how iron oxides are distributed into particles, there are few observations to test our default configuration. Thus, this second scheme tests the sensitivity of the dust DRE to the assumed mixing state of iron oxides with the other minerals.

    Both the EXT and INT coupling schemes relate the CRI to mineral composition in only the UV-VIS band of the radiation module of ModelE2.1 $(0.30-0.77\,\mu m)$, where in contrast we assume globally homogeneous composition in the HOM scheme
175    (see below). Slightly more than half of total insolation at TOA is within this band, where recent measurements from DB19 show that most SW absorption by dust occurs (Section 2.2.3). In the remaining five NIR bands of the SW spectrum (covering

wavelengths from $0.77$ to $4\,\mu m$), we use unspeciated dust optical properties that are identical in all our experiments. We calculate the default homogeneous properties using a globally uniform CRI prescribed by smoothly joining the IRI retrieved by Sinyuk et al. (2003) at UV-VIS wavelengths with values reported by Volz (1973) at wavelengths longer than $2.5\,\mu m$,

180 extending into the longwave (LW) bands. Similarly, for the RRI, values from Patterson et al. (1977) at UV-VIS wavelengths are smoothly joined to the values from Volz (1973) in the LW spectrum. In the control experiment (HOM), we use the default CRI for all minerals also in the UV-VIS band, thus prescribing homogeneous composition. In this work, we do not update the calculation of dust optical properties in the LW bands, and use the default properties of the model that explicitly only account for dust absorption. To represent the effect of LW scattering the extinction is increased by $30\,\%$ (Miller et al., 2006). Moreover,

185 in all the optical calculations conducted in this work we assume spherical shape for dust particles.
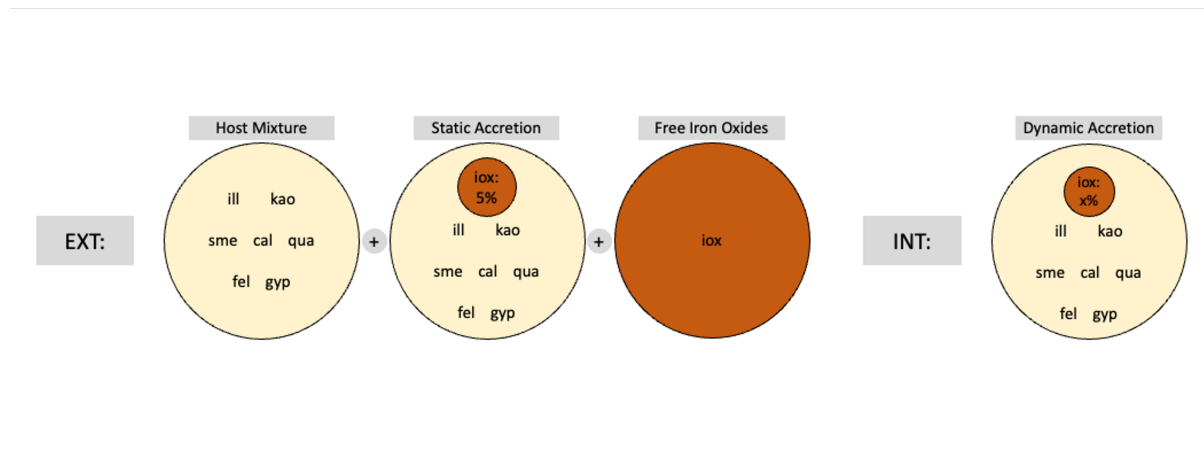
**Figure 1.** Schematic cartoon of the mixing state of minerals, assumed for optical calculations, in the coupling schemes with external (EXT) and internal (INT) mixing configuration. The EXT scheme assumes external mixing of three mineral components, whose size-resolved proportions vary in space and time: 1) a homogeneous amalgam of non iron-oxide minerals (host mixture), 2) a two-component mixture of the host amalgam and a fixed $5\,\%$ mass fraction of iron oxides (static accretion), and 3) free iron oxides. In the INT scheme, the fifteen mineral tracers are re-arranged to form a single size-resolved internal mixture of the host amalgam with a mass fraction of iron oxides that varies at each grid box and time step (indicated as $x\,\%$). The acronyms for minerals indicate: illite ('ill'), kaolinite ('kao'), smectite ('sme'), calcite ('cal'), quartz ('qua'), feldspar ('fel'), gypsum ('gyp') and iron oxides ('iox').

### 2.2.2 Complex refractive index of host mixture

In the EXT scheme, we need the CRI for the radiative component consisting of host minerals (host mixture), which we also use as the CRI for the either static (EXT) or dynamic (INT) accretion in the limit of vanishing iron oxides. SZ15 showed that differences in the CRI of individual non-iron oxide minerals across solar wavelengths are irrelevant compared to their contrast with the iron oxide CRI. Thus, we derive a globally uniform CRI for the host amalgam, neglecting the regional variations in

190 the soil fractions of host minerals. We apply a mixing rule to the individual CRIs of the seven host minerals (taken from SZ15;

Figure 2) according to the mass fractions of the same minerals in eighteen dust aerosol samples measured by DB19 (reported in the supplement of Di Biagio et al., 2017). (We exclude the 'Taklimakan' sample of DB19 because measurements of iron oxides were not reported for this sample.) Among the common mixing rules for calculating the CRI of particles composed of different
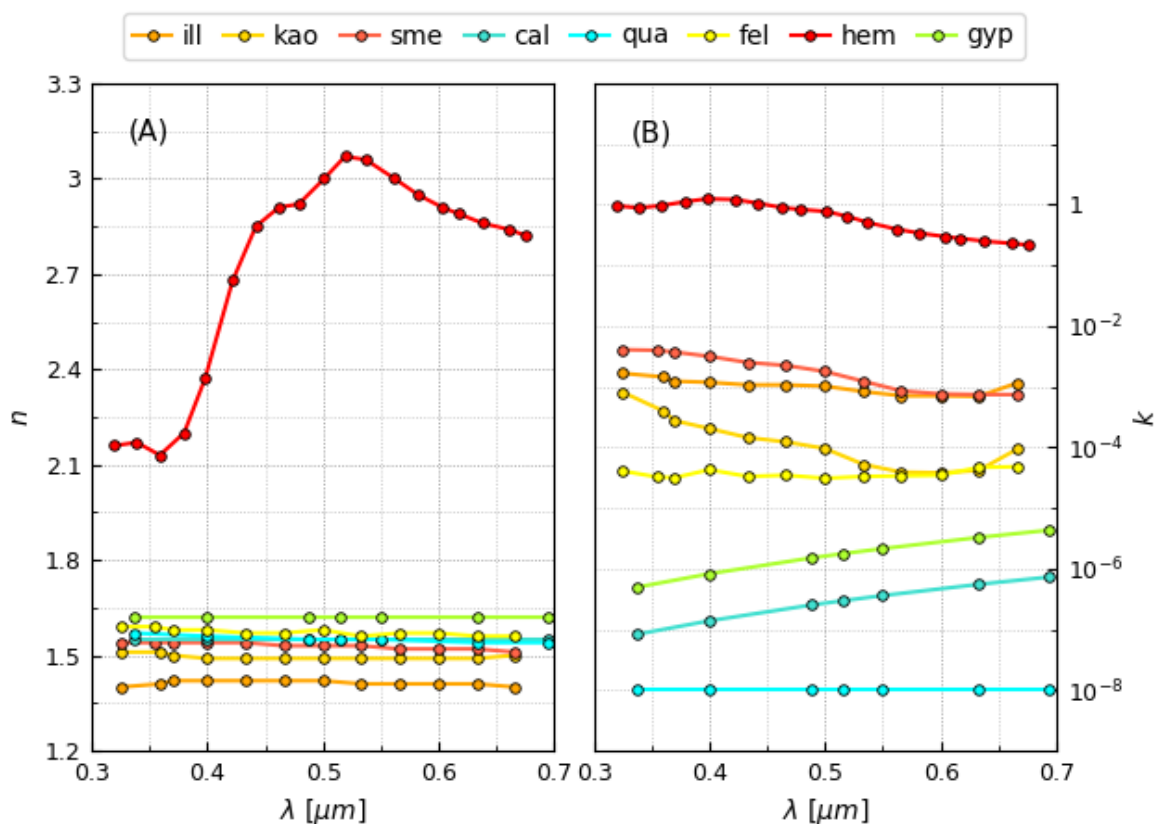
**Figure 2.** Real ($n$; A) and imaginary ($k$; B) indices of single minerals at visible wavelengths ($\lambda$) as collected by Scanza et al. (2015): illite ('ill'), kaolinite ('kao'), smectite ('sme'), calcite ('cal'), quartz ('qua'), feldspar ('fel'), hematite ('hem') and gypsum ('gyp').

195 constituents, 'homogenization theories' such as the MG (Maxwell Garnett) and the BG (Bruggeman) methods (Markel, 2016) are consistent with Maxwell's electromagnetism equations. MG assumes the particle to be composed of a homogeneous host material filled with small inclusions of contrasting composition, but its application is challenged by the requirement that the total volume fraction of the inclusions must be much lower than the host volume fraction (Markel, 2016). BG generalizes MG to a particle morphology in which the inclusions virtually occupy the entire particle volume (and the host disappears), but for

200 combinations of more than two minerals numerical methods are required for calculating the physical solution (Markel, 2016). Given these difficulties, we calculate the CRI of the host mixture using the empirical VM (volume-weighted mean) rule, which prescribes the real and imaginary parts of the composite CRI in proportion to the volume fractions of each mineral. While VM predicts greater absorption compared to MG or BG when the inclusion is highly absorbing, this bias is less important for the amalgam of host minerals whose absorption is small compared to that of iron oxides.

To obtain the CRI of the host mixture, we first calculate mineral volume fractions from the mass fractions in the DB19 samples, using the mass density of individual host minerals as prescribed in ModelE2.1 (Table 1). We then apply the VM rule to each sample and calculate the mean across all samples. We perform this calculation at the seven solar wavelengths of DB19 (Figure 3) after interpolating the mineral CRIs from SZ15 at these wavelengths. Importantly, we find a very good agreement between our calculated host mixture IRI and the IRI retrieved by DB19 in the samples with iron oxide fractions approaching to zero. For example, in the Bodélé sample, whose measured mass fraction of iron oxides is $0.7\%$, DB19 retrieved an IRI of $0.0007$ and $0.0004$ at $0.470$ and $0.590\,\mu m$, respectively. At the same wavelengths, our VM calculation for the host mixture gives $0.00077$ and $0.00035$, respectively. This agreement (within the experimental errors of DB19) gives us confidence in our independent derivation of the IRI for the host mixture and allows us to use it as the base for the calculation of the accretion IRI.

### 2.2.3 Complex refractive index of accretions

We model our static and dynamic accretions as two-component particles consisting of the host mixture plus a small fraction of iron oxides. We calculate the IRI of these accreted particles using the IRI for the host amalgam (derived above) plus a perturbation that is proportional to the either fixed (static accretion) or varying (dynamic accretion) mass fraction of iron oxides. This approach is suggested by the empirical relation of dust IRI to the content of iron oxides measured by DB19, and allows us to circumvent choosing a hematite IRI from the large range reported in the literature (e.g. Zhang et al., 2015) along with a single mixing rule to approximate the wide variety of mineral physical arrangements within dust particles.

At each measurement wavelength of DB19, we perform a third-order polynomial fit to their IRI retrievals versus the mass fraction of iron oxides in their samples (Figure 3). The polynomial fit is constructed to match the host mixture IRI (Section 2.2.2) in the limit of vanishing iron oxide mass fraction, while reducing the low bias of a linear fit at larger fractions. We define a suitable fitting function as the third-order Maclaurin expansion of an exponential function in the mass fraction of iron oxides ($m_{iox}$):

$$k_{acc} = k_{hos}e^{p_1 m_{iox}} \approx k_{hos}(1 + p_1 m_{iox} + \frac{p_1^2}{2}m_{iox}^2 + \frac{p_1^3}{6}m_{iox}^3), \tag{1}$$

where $k_{acc}$ and $k_{hos}$ indicate the IRI of the accretion and host amalgam, respectively, and $p_1$ is the best fit parameter defining the fitting function. DB19 also reported relationships of dust IRI with respect to the separate mass fractions of hematite, goethite or total iron (including iron from non-iron oxide minerals like phyllosilicates). We use the total iron oxide mass as the independent variable, because DB19 found a more robust relationship using hematite and goethite together rather than these minerals separately. As already stated (Section 2.1), while only hematite is prescribed in the soil mineralogy of Claquin et al. (1999) and implemented in ModelE2.1 (Perlwitz et al., 2015a), we assume, as a first approximation, that hematite is a proxy for both iron oxides.

Perturbations of RRI due to iron oxides are less critical to our results, as dust absorption and DRE are mostly sensitive to the IRI. Moreover, given that typical fractions of accreted iron oxides are small, different mixing rules for RRI would result in similar RRI for the accretion. For example, the absolute difference in RRI is $\lesssim 0.005$ between VM and MG for iron oxide mass fractions $\lesssim 6\%$ (Figure A1-B). Given this insensitivity, we apply a simple two-component VM rule for the accretion RRI
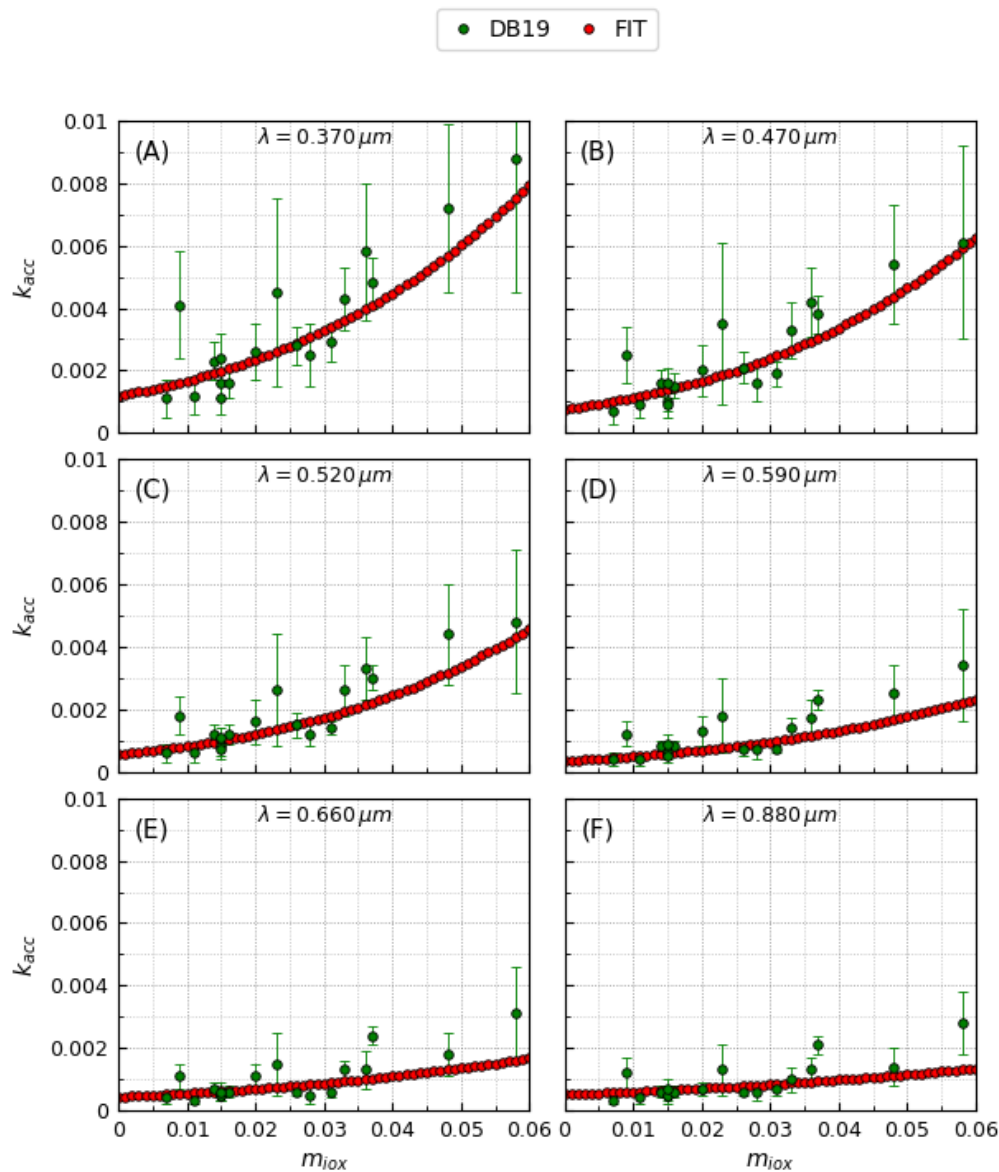
**Figure 3.** Polynomial fits (FIT) of dust imaginary indices ($k_{acc}$) retrieved by Di Biagio et al. (2019) (DB19) versus the mass fraction of iron oxides in the dust aerosol samples ($m_{iox}$), including both hematite and goethite. The fits are calculated at the seven shortwave wavelengths ($\lambda$) of DB19: 0.370, 0.470, 0.520, 0.590, 0.660, 0.880 and 0.950 $\mu m$ (the last wavelength is not shown here). The intercepts of the polynomial fitting function are set to the imaginary index of the host mixture (Section 2.2.2).

($n_{acc}$), using the hematite RRI from SZ15 for iron oxides ($n_{iox}$):

$$n_{acc} = n_{hos} + (n_{iox} - n_{hos})v_{iox}, \tag{2}$$

240    where $n_{hos}$ indicates the RRI of the host amalgam, and $v_{iox}$ is the either static (EXT) or dynamic (INT) volume fraction of accreted iron oxides.

### 2.2.4   Complex refractive index of free iron oxides

In the EXT scheme, we also assign a CRI to the radiative component comprised of crystalline or free iron oxides. As the RRI, we use the hematite value from SZ15, as already mentioned in Section 2.2.3. Given the large range of literature values (e.g.
245    Zhang et al., 2015), we choose instead to derive a new IRI consistent with the measurements of DB19 through an inverse calculation. This inversion requires a mixing rule to relate the retrieved IRI of composite particles to that of embedded iron oxides. Because free iron oxides make only a small contribution to the total dust extinction in the EXT scheme (Section 3.1.2), the specific CRI that we assign to this component is nearly irrelevant to our results. Therefore, we defer our derivation of the iron oxide IRI to Appendix A. Nonetheless, in Figure 4 we compare our calculated IRI, reflecting the presence of both hematite
250    and goethite in the DB19 samples, to literature values for hematite and goethite. Our estimate is roughly intermediate between hematite and goethite IRIs measured by Bedidi and Cervelle (1993) that, to our best knowledge, is the only work reporting goethite IRI at VIS wavelengths. Other estimates of the IRI for hematite alone are much higher than our values, especially towards short-VIS wavelengths. This discrepancy may be due to different measurement techniques and samples as well as the presence of goethite in the DB19 samples.

255    ### 2.3   Filtering dust events in AERONET

In order to evaluate our model calculations, we filter hourly AERONET data (Version 3; Sinyuk et al., 2020) to identify scenes where dust is the dominant aerosol and generate monthly climatologies of aerosol optical depth (AOD) and SSA (among other inversion variables) over the 2000–2020 period at the four wavelengths of the Almucantar scan (0.440, 0.675, 0.870, 1.020 $\mu m$). One of the quality assurance criteria applied to produce the Level 2.0 inversion product (Holben et al., 2006) is
260    a threshold for AOD at 0.440 $\mu m$: $\tau_{440} > 0.4$, which assures a relatively small error of the inversion variables but excludes the bulk of data in many stations (Li et al., 2014). We generate two observational data sets to compare different variables: for SSA we use Level 2.0 data, whereas for DOD we apply to Level 1.5 data all of the high-quality Level 2.0 criteria except the threshold for AOD at 0.440 $\mu m$. These two data sets include a different number of stations and available months, and are indicated hereafter as AeroTAU4 ($\tau_{440} > 0.4$) and AeroTAU0 ($\tau_{440} > 0$).

265    Our approach for filtering dust measurements uses both size and the spectral absorption features of the common tropospheric aerosol species, and aims to improve the widely used technique based only on the differences in size among species. The volume size distribution of mineral dust typically presents a pronounced coarse mode (particle diameter: $d \gtrsim 1.2\,\mu m$) especially near dust sources (Dubovik et al., 2002), whereas the fine mode is mainly populated by other species such as BC, BrC, non-absorbing organics, sulfates and nitrates. We therefore first reduce the contribution of fine species by imposing a maximum for the fine-
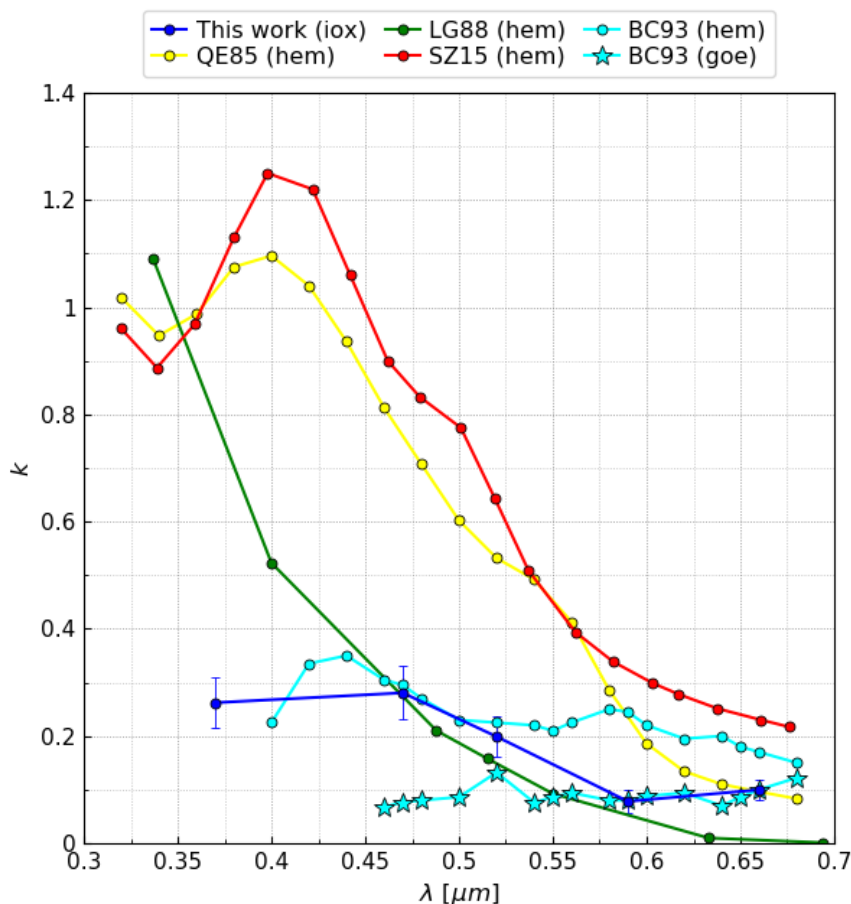
**Figure 4.** Imaginary index ($k$) of iron oxides ('iox') calculated in this work and literature values for hematite ('hem') and goethite ('goe') at visible wavelengths ($\lambda$). The references are Querry (1985) (QE85), Longtin et al. (1988) (LG88), Scanza et al. (2015) (SZ15), Bedidi and Cervelle (1993) (BC93).

270    volume fraction (FVF): $v_{fin} < 0.1$. Separating dust from fine species is a fundamental first step but a pronounced coarse mode may also indicate sea salt, especially in coastal stations (note that in the AeroTAU4 data set, the threshold for AOD at $0.440\,\mu m$ should filter out most scenes dominated by coarse sea salt, whose load does not generate often $\tau_{440} > 0.15$; Dubovik et al., 2002). Moreover, small amounts of highly absorbing carbonaceous species may contaminate the measurements, obscuring absorption by dust. To address these issues, in addition to the size filter, we use the known spectral absorption features of the

275    different aerosol species at solar wavelengths.

     Dubovik et al. (2002) showed that the aerosol mixtures observed by AERONET photometers typically exhibit decreasing or nearly constant SSA at UV-VIS wavelengths. In the case of mixtures dominated by fine anthropogenic species, negative SSA slopes may be attributable to size effect (the scattering efficiency peaks at wavelengths similar to particle size; Hansen and

Travis, 1974) as well as the presence of BC which significantly absorbs also at long-VIS wavelengths (Kirchstetter et al., 2004).
In the case of pure oceanic aerosol, the nearly flat wavelength dependence of SSA is due to the substantially null absorption
capability of sea salt in the UV-VIS-NIR spectrum. In contrast, mineral dust is the only species whose SSA increases between
$0.440$ and $0.675\,\mu m$ (Dubovik et al., 2002), because dust aerosols are significantly composed of coarse particles and also
because iron oxides are known to absorb mainly at UV and short-VIS wavelengths (Zhang et al., 2015; Bedidi and Cervelle,
1993). So, to further reduce contamination by non-dust species, we require the SSA to increase through UV-VIS wavelengths
(Ginoux et al., 2010): $\omega_{675} - \omega_{440} > 0$.

Even after this filtering, small remaining fractions of absorbing carbonaceous species may still alter the absorption capability
of the mixture dominated by dust. This may happen for two reasons. First, BC and BrC particles from biomass burning
and industrial/urban combustion sources have been actually found attached to dust particles (Derimian et al., 2008; Hand
et al., 2010). Second, the inversion algorithm of AERONET assumes a homogeneous internal mixture of aerosols, without
distinguishing between fine and coarse modes (i.e. only one CRI is retrieved for both modes): this potentially causes absorption
by fine particles to be artificially shared with the coarse mode (Schuster et al., 2016). To reduce this effect, we follow Schuster
et al. (2016) and apply our third condition: $k_{rir} < 0.0042$, where $k_{rir}$ is the mean IRI at $0.675$, $0.870$ and $1.020\,\mu m$ and the
value of $0.0042$ is a threshold defined by Schuster et al. (2016) to separate 'pure' dust from 'pure' biomass burning species
in AERONET retrievals. (Note that the threshold of $0.0042$ is also consistent with the IRI retrievals of DB19.) This condition
directly detects the presence of BC, which is the only species absorbing at these wavelengths (Kirchstetter et al., 2004), but
indirectly filters out primary BrC that is expected to coexist with BC as a byproduct of the same combustion processes. Our
combination of filters aims to select measurements strongly dominated by mineral dust, but it must be pointed out that removing
all contributions by non-dust species in the AERONET observations is impossible.

We calculate monthly means of DOD and SSA (in AeroTAU0 and AeroTAU4 data sets, respectively) considering only
stations that provide more than $80$ hourly measurements per month (over the whole 2000–2020 period), for at least one month,
after the multiple filtering. From the monthly values at the four AERONET wavelengths, we average DOD and SSA in the
UV-VIS band of ModelE2.1 ($0.30 - 0.77\,\mu m$) by applying the same procedure used for the model properties (see Appendix
B2). Note that we always calculate DOD-weighted means for both model and observed SSA. All the thirty-eight (AeroTAU0)
and twenty-seven (AeroTAU4) stations selected through our filtering method are listed with their coordinates in Table 2, and
plotted within nine and six regions, for AeroTAU0 and AeroTAU4, respectively, in Figure 5. To compare model variables to
AERONET observations, we first derive the model monthly means at the selected stations and then mask them to remove those
months not included in the observational sample.

## 3 Results

In the following Section 3.1 we show the results of our model calculations, analyzing the changes to DOD, SSA and DRE due
to the varying mineral composition compared to default homogeneously composed dust, and the sensitivity of these variables

**Table 2.** Selected AERONET stations with coordinates, divided by region (Figure 5). All listed stations are included in the AeroTAU0 data set, while the ones also included in AeroTAU4 are marked with a 'x'.

| Station | Region | Latitude | Longitude | AeroTAU4 |
|---|---|---|---|---|
| Capo_Verde | N.W. AFRICA | 16.73 | −22.94 | x |
| Granada | | 37.16 | −3.61 | |
| Izana | | 28.31 | −16.50 | |
| La_Laguna | | 28.48 | −16.32 | x |
| Ouarzazate | | 30.93 | −6.91 | |
| Saada | | 31.63 | −8.16 | x |
| Santa_Cruz_Tenerife | | 28.47 | −16.25 | x |
| Tamanrasset_INM | | 22.79 | 5.53 | x |
| Teide | | 28.27 | −16.64 | |
| Eilat | N.E. AFRICA | 29.50 | 34.92 | |
| El_Farafra | | 27.06 | 27.99 | |
| KAUST_Campus | | 22.30 | 39.10 | x |
| Medenine-IRA | | 33.50 | 10.64 | x |
| SEDE_BOKER | | 30.85 | 34.78 | x |
| Agoufou | SAHEL | 15.35 | −1.48 | x |
| Banizoumbou | | 13.55 | 2.67 | x |
| Dakar | | 14.39 | −16.96 | x |
| DMN_Maine_Soroa | | 13.22 | 12.02 | x |
| IER_Cinzana | | 13.28 | −5.93 | x |
| Ilorin | | 8.48 | 4.67 | x |
| Ouagadougou | | 12.42 | −1.49 | x |
| Zinder_Airport | | 13.78 | 8.99 | x |
| Hamim | A. PENINSULA | 22.97 | 54.30 | x |
| Kuwait_University | | 29.33 | 47.97 | x |
| Mezaira | | 23.10 | 53.75 | x |
| Mussafa | | 24.37 | 54.47 | x |
| Solar_Village | | 24.91 | 46.40 | x |
| Gandhi_College | N. INDIA | 25.87 | 84.13 | x |
| Jaipur | | 26.91 | 75.81 | x |
| Kanpur | | 26.51 | 80.23 | x |
| Karachi | | 24.95 | 67.14 | x |
| Lahore | | 31.48 | 74.26 | x |
| Dushanbe | C. ASIA | 38.55 | 68.86 | x |
| IASBS | | 36.71 | 48.51 | |
| Cape_San_Juan | CARIBBEAN | 18.38 | −65.62 | |
| La_Parguera | | 17.97 | −67.05 | |
| Trelew | PATAGONIA | −43.25 | −65.31 | |
| Tinga_Tingana | AUSTRALIA | −28.98 | 139.99 | |
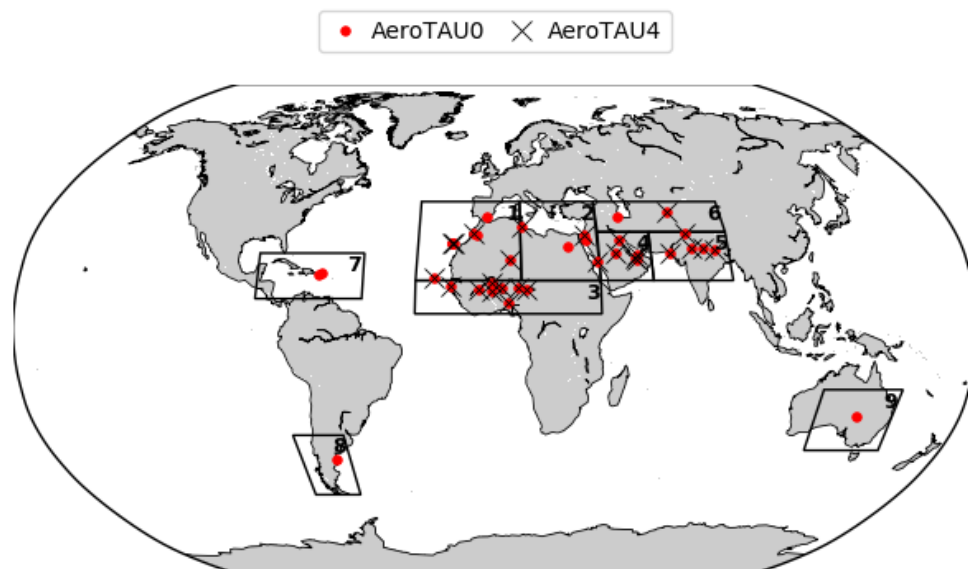
**Figure 5.** AERONET stations selected by filtering dust events, located within dust regions: (1) northwestern Africa, (2) northeastern Africa, (3) Sahel, (4) Arabian Peninsula, (5) northern India, (6) central Asia, (7) Caribbean, (8) Patagonia, (9) Australia. Stations included in the AeroTAU0 data set (optical depth: $\tau_{440} > 0$) are located in all nine regions; stations in the AeroTAU4 data set ($\tau_{440} > 0.4$) are located only within the first six source regions.

to the mixing configuration assumed for minerals. In Section 3.2, we compare the modeled dust optical properties (SSA and DOD), calculated with the two different optical schemes, to AERONET observations in the selected stations and months.

## 3.1 Mineralogy effect upon dust optical properties and direct radiative effect

### 3.1.1 Evaluation of default homogeneously composed dust (HOM)

315 In Figure 6, we show annual mean DOD, SSA and (all-sky) DRE at TOA and at surface (SFC), as calculated in the control run (HOM), that assumes globally homogeneous mineral composition. The optical properties (DOD and SSA) are averaged over the UV-VIS band of ModelE2.1 ($0.30 - 0.77 \, \mu m$) whereas the DRE is for the entire SW spectral region. Our model simulates the highest DOD (Figure 6-A) in northern Africa and the Sahel, including dust plumes downwind over the Atlantic Ocean, along with the Arabian Peninsula (DOD up to $0.91$), while lower values are calculated in northern India, central Asia and

320 Australia. In Figure 6-B, our default dust, whose IRI at UV-VIS wavelengths is from Sinyuk et al. (2003), shows SSA between $\sim 0.90$ and $\sim 0.93$ in the main dust source regions, and increasing SSA downwind from the sources, indicating enhanced scattering due to the shorter lifetime of more absorbing large particles (Table 3) that are preferentially removed by gravitational settling (Miller et al., 2006). The DRE at TOA, in Figure 6-C, shows a typical contrasting pattern with negative values above
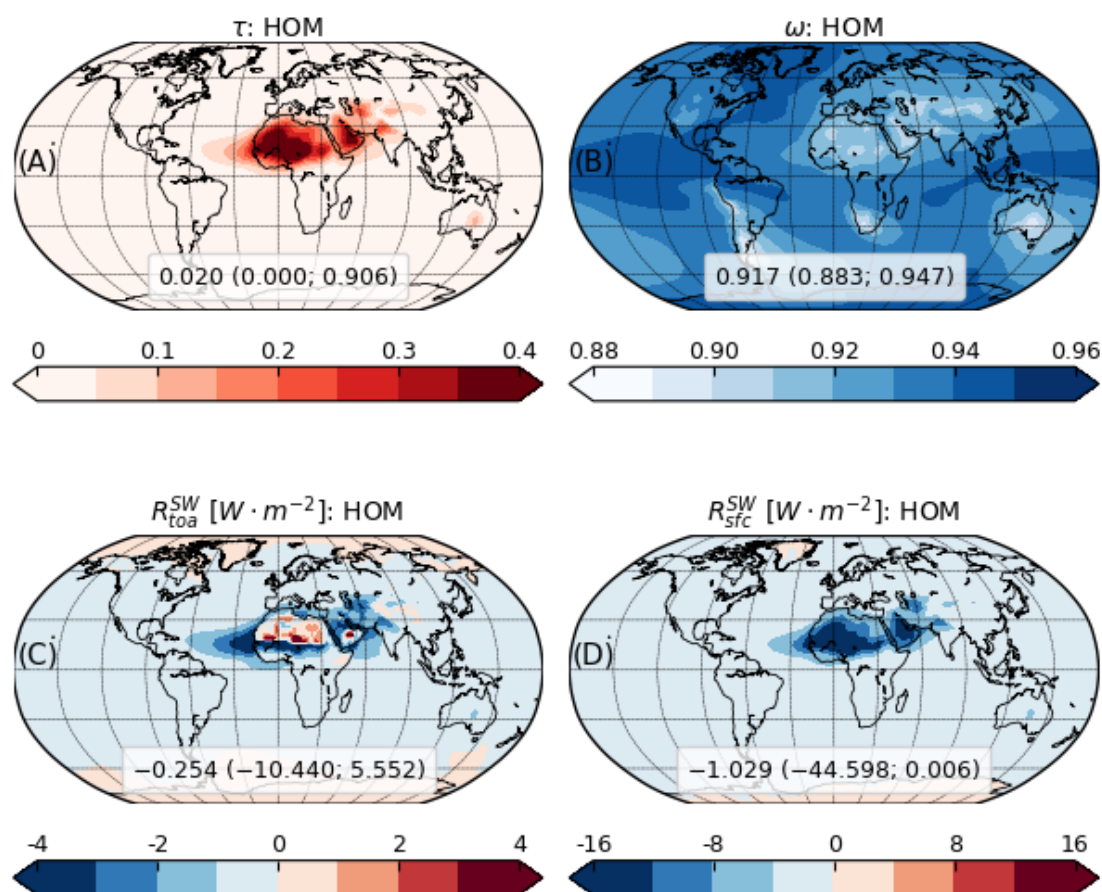
**Figure 6.** Annual mean optical depth ($\tau$; A), single scattering albedo ($\omega$; B), direct radiative effect at the top of atmosphere ($R^{SW}_{toa}$; C) and at surface ($R^{SW}_{sfc}$; D), from the control run with homogeneous composition (HOM). The optical properties are averaged over the spectral band of ModelE2.1 covering ultra-violet and visible wavelengths ($0.30 - 0.77\,\mu m$), while the direct radiative effect is relative to the entire shortwave spectrum ($0.30 - 4\,\mu m$). The extremes of the color bars are set to include $1^{st}$ and $99^{th}$ percentiles of the mapped variables. Note that the color mapping for single scattering albedo indicates higher scattering (relative to extinction) with more intense blue. Global average along with minimum and maximum (within parentheses) are also reported.

dark oceanic and vegetated areas, and null or slightly positive values (with peaks in specific areas) over bright desert surfaces.
325 Finally, dust has a cooling effect everywhere at SFC (Figure 6-D).

**Table 3.** Global emission rate ($E$: annual total), global mass load ($L$: annual mean) and size-resolved lifetime ($T$), along with global-annual mean optical depth ($\tau$), single scattering albedo ($\omega$), and direct radiative effect at the top of atmosphere ($R_{toa}^{SW}$) and at surface ($R_{sfc}^{SW}$), of model dust from the control run with homogeneous composition (HOM) and the mineral experiments with external (EXT) and internal (INT) mixing configuration for minerals. PM$_{20}$ estimates for emission rate ($E_{20}$), mass load ($L_{20}$) and optical depth ($\tau_{20}$), calculated by assuming a constant sub-bin volume size distribution on logarithmic scale (see Appendix B2), are also reported. The optical properties are averaged over the spectral band of ModelE2.1 covering ultra-violet and visible wavelengths ($0.30 - 0.77 \, \mu m$), while the direct radiative effect is relative to the entire shortwave spectrum (SW: $0.30 - 4 \, \mu m$). For completeness, also the direct radiative effect relative to longwave bands is reported ($R_{toa}^{LW}$ and $R_{sfc}^{LW}$, at the top of atmosphere and surface, respectively). For each variable, the mean and standard error (within parentheses) over the simulation period (1991–2020) are reported.

| Variable | HOM | EXT | INT |
|---|---|---|---|
| $E \; [Tg \cdot y^{-1}]$ | 6145.8 (47.9) | 6331.4 (48.9) | 6532.1 (63.2) |
| $E_{20} \; [Tg \cdot y^{-1}]$ | 4030.5 (27.3) | 4152.0 (27.9) | 4283.6 (36.0) |
| $L \; [Tg]$ | 33.778 (0.316) | 35.031 (0.330) | 36.424 (0.409) |
| $L_{20} \; [Tg]$ | 31.296 (0.285) | 32.437 (0.300) | 33.740 (0.371) |
| $T \; [d]$ | Clay-1: 7.13 | Clay-1: 7.13 | Clay-1: 7.21 |
| | Clay-2: 7.13 | Clay-2: 7.13 | Clay-2: 7.21 |
| | Clay-3: 7.13 | Clay-3: 7.13 | Clay-3: 7.21 |
| | Clay-4: 7.13 | Clay-4: 7.13 | Clay-4: 7.21 |
| | Silt-1: 6.45 | Silt-1: 6.45 | Silt-1: 6.52 |
| | Silt-2: 4.89 | Silt-1: 4.91 | Silt-2: 4.96 |
| | Silt-3: 2.17 | Silt-1: 2.20 | Silt-3: 2.21 |
| | Silt-4: 0.43 | Silt-1: 0.43 | Silt-4: 0.44 |
| $\tau$ | 0.0199 (0.0002) | 0.0207 (0.0002) | 0.0215 (0.0003) |
| $\tau_{20}$ | 0.0197 (0.0002) | 0.0204 (0.0002) | 0.0213 (0.0002) |
| $\omega$ | 0.917 (0.001) | 0.936 (0.001) | 0.942 (0.001) |
| $R_{toa}^{SW} \; [W \cdot m^{-2}]$ | $-0.254$ (0.003) | $-0.302$ (0.003) | $-0.337$ (0.005) |
| $R_{toa}^{LW} \; [W \cdot m^{-2}]$ | 0.176 (0.002) | 0.183 (0.002) | 0.191 (0.002) |
| $R_{sfc}^{SW} \; [W \cdot m^{-2}]$ | $-1.029$ (0.010) | $-0.975$ (0.010) | $-0.995$ (0.013) |
| $R_{sfc}^{LW} \; [W \cdot m^{-2}]$ | 0.629 (0.006) | 0.646 (0.007) | 0.678 (0.008) |

As reported in Table 3, in the control run, the global emission rate is $6146 \, Tg \cdot y^{-1}$, which reduces to $4030 \, Tg \cdot y^{-1}$ as the PM$_{20}$ value, which we estimate by including all bins covering diameters below $16 \, \mu m$ and a fraction of the coarsest bin ($16 - 32 \, \mu m$ in diameter; Table B2) calculated assuming a constant sub-bin volume size distribution on logarithmic scale, the same we use for optical calculations (see Appendix B2). In Figure 7-A, we show that roughly half of the emitted dust mass

330 is from the coarsest bin, which is consistent with our enhanced emission at large sizes (Section 2.1). Particles in our coarsest bin settle very rapidly (lifetime is $0.43$ days; Table 3), decreasing the global mass load in the coarsest bin (Figure 7-B) to $11\%$ of the bulk mass load ($34\,Tg$; Table 3). Despite this reduction, our model reproduces fairly well ($18\,Tg$) the mass load constrained by Adebiyi and Kok (2020) in the coarse diameter range of $5-20\,\mu m$: $17\,Tg$ ($10-29\,Tg$). This likely results from our enhanced emission at large sizes compensating the rapid deposition of coarse particles that may be excessive compared to

335 observations (van der Does et al., 2016). On the other hand, our $PM_{20}$ mass load ($31\,Tg$; Table 3) is close to the high end of the range constrained by Kok et al. (2017) ($14-33\,Tg$), mostly due to their smaller mass load in the coarse diameter range of $5-20\,\mu m$ ($10\,Tg$ as reported by Adebiyi and Kok, 2020). In contrast, our global mean DOD ($0.020$ also for $PM_{20}$; Table 3) equals the lowest value of the range used by Kok et al. (2017) ($0.02-0.04$ at $0.550\,\mu m$, as constrained by Ridley et al., 2016). This indicates that our modeled dust has low mass extinction efficiency with respect to observational constraints, given

340 that compared to Kok et al. (2017) (as well as to Adebiyi and Kok, 2020) we have similar mass load for diameters below $5\,\mu m$ (Figure 3 of Adebiyi and Kok, 2020). This mismatch may partly be due to the enhanced extinction efficiency of tri-axial ellipsoids assumed by Kok et al. (2017) compared to our assumed spheres.

Our global mean DRE at TOA is $-0.25\,W\cdot m^{-2}$ (Table 3). This value indicates lower cooling by dust compared to Klose et al. (2021), who calculated a DRE of $-0.41\,W\cdot m^{-2}$ for the SW, with a DOD of $0.036$ at $0.550\,\mu m$. Adjusting our DRE

345 to the same DOD, through our DRE efficiency of $-12.75\,W\cdot m^{-2}$, results in a similar value of $-0.45\,W\cdot m^{-2}$. We have a more negative DRE efficiency compared to the value of $-11.55\,W\cdot m^{-2}$ by Klose et al. (2021), despite our lower SSA ($0.917$ versus $0.953$): this is probably attributable to modeling differences such as for example the spectral dependence of DOD in the UV-VIS band (note that our DOD is calculated as a band average) or the assumed surface albedo. On the other hand, our DRE at TOA adjusted to the DOD of $0.03$ (central value of the range from Ridley et al., 2016) is $-0.38\,W\cdot m^{-2}$, which remains

350 closer to the less cooling end of the range constrained by Kok et al. (2017) for $PM_{20}$ dust (from $\sim-0.80$ to $\sim-0.15\ \ W\cdot m^{-2}$ for the SW). This may partly be due to the warming effect of the coarsest particles in our full-size calculation (Figure 7-B), which are underrepresented (Adebiyi and Kok, 2020) or not included (i.e. diameters above $20\,\mu m$) in Kok et al. (2017). Likely for the opposite reason, our DRE efficiency is significantly more negative compared to the value of $-9.62\,W\cdot m^{-2}$ estimated by Di Biagio et al. (2020), despite our DRE of $-0.25\,W\cdot m^{-2}$ equals their estimate ($-0.25\pm0.21\,W\cdot m^{-2}$ for the SW, with

355 a DOD of $0.026$ at $0.550\,\mu m$). Di Biagio et al. (2020) extended the emitted PSD to diameters above $20\,\mu m$ (up to $150\,\mu m$) by fitting airborne measurements from the FENNEC campaign (Ryder et al., 2013a, b): the warming effect of their giant particles, whose diameters are not included in our model, may partly explain their less negative DRE efficiency.

### 3.1.2 Effect of externally mixed mineral components (EXT versus HOM)

In Figure 8, we show the effect of regionally varying soil mineral composition upon annual DOD and SSA in the UV-VIS
360 band, and the all-sky DRE at TOA and at SFC for the entire SW spectrum, assuming an external mixture of three radiatively active mineral components (EXT) with respect to HOM. Accounting for mineralogy enhances the extinction (Figure 8-A), while reducing the global absorption (Figure 8-B), with a global mean DOD contrast of $+3.6\%$ and the global mean SSA increasing from $0.917$ to $0.936$ (Table 3). In general, reducing absorption with fixed mass would increase the SSA but leave
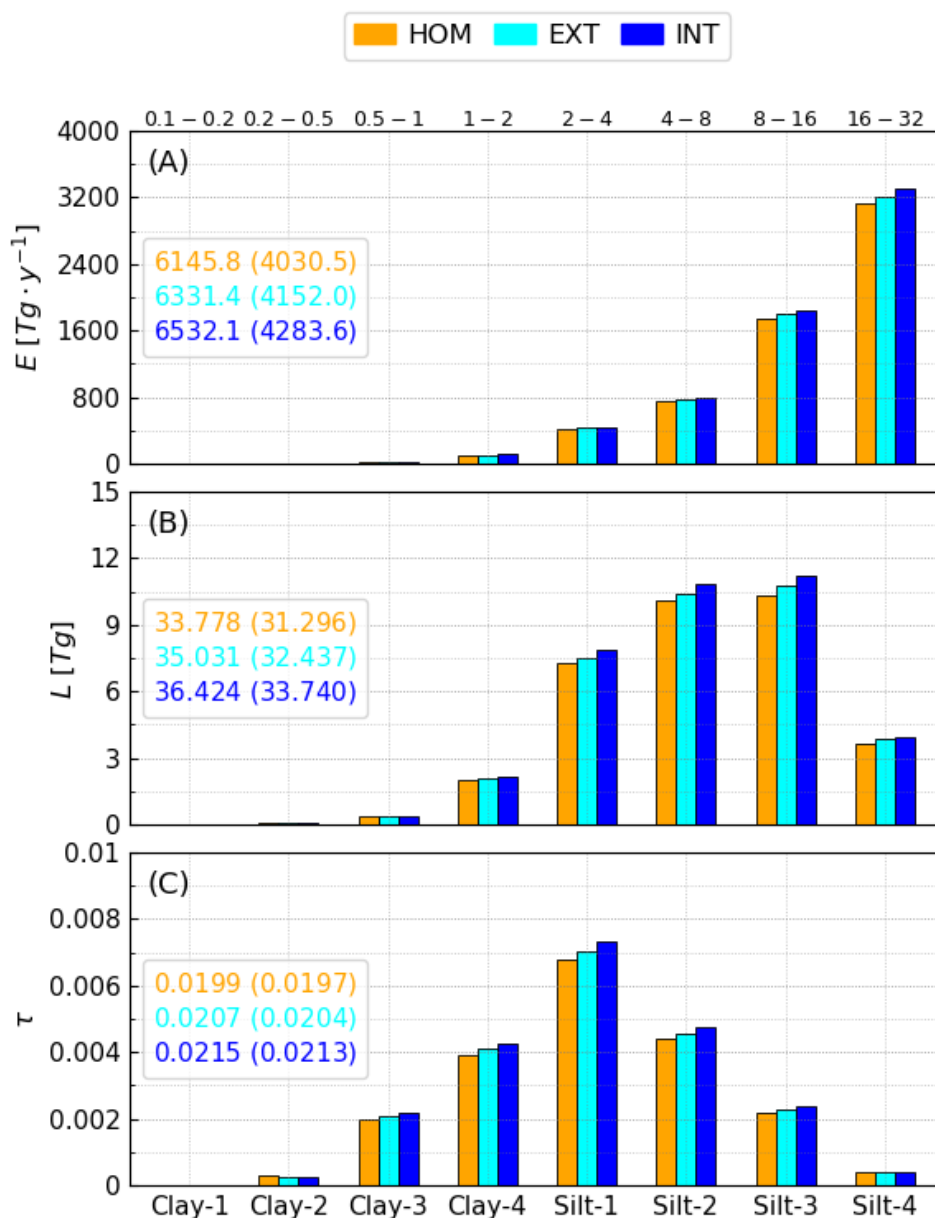
**Figure 7.** Size-resolved global emission rate ($E$: annual total; A), global mass load ($L$: annual mean; B) and global-annual mean optical depth ($\tau$; C) of model dust from the control run with homogeneous composition (HOM) and the mineral experiments with external (EXT) and internal (INT) mixing configuration. The optical depth is averaged over the spectral band of ModelE2.1 covering ultra-violet and visible wavelengths ($0.30 - 0.77\,\mu m$). The ranges reported on the upper $x$-axis of the top panel indicate the diameters (expressed in $\mu m$) covered in each size bin (Table B2). Within each panel, the bulk values (sums over all bins) and our estimates for the $PM_{20}$ range (within parentheses) are reported for each experiment (Table 3).
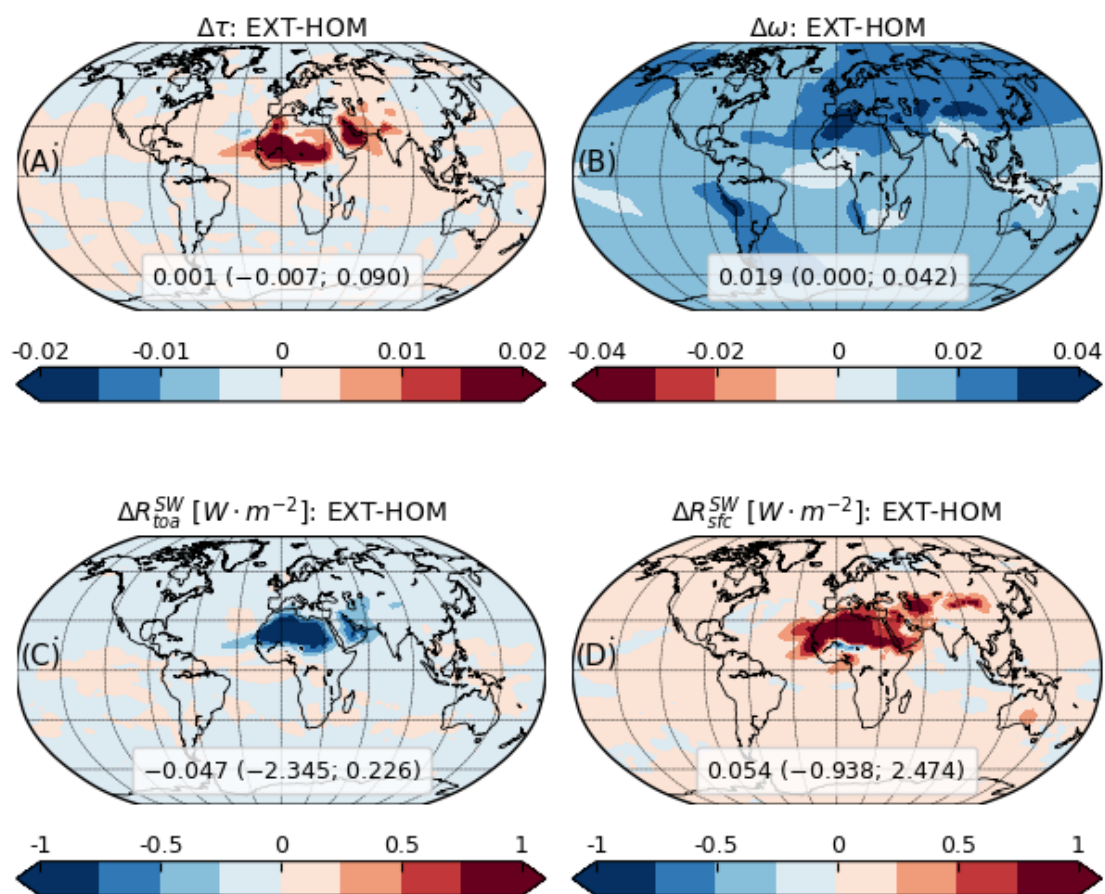
**Figure 8.** Same as Figure 6 but showing the contrast between the mineral experiment with external mixing configuration (EXT) and the control run with homogeneous composition (HOM). Note that the color mapping for single scattering albedo indicates increased/decreased scattering with blue/red.

the extinction almost unaffected (e.g. Figure 9.7 of Mishchenko et al., 2002). In Figure 9-C, we show that the DOD increase

365   due solely to distinguishing the CRI of the three mineral components would be substantially negligible ($\lesssim 0.5\,\%$ with respect to Figure 6-A over most source regions) compared to the DOD contrast in Figure 8-A. The latter, therefore, can be attributed to differences in aerosol mass between the EXT and HOM experiments. Despite identical calibration of the emitted mass as a function of wind speed, mass variations indicate a changed radiative feedback upon global emission and thus the mass load, whose contrast of $+3.7\,\%$ is consistent with that of the global mean DOD. Also, in Figure 9-B we show the column mass

370   load (annual mean) in the EXT simulation with respect to the smaller load in HOM (Figure 9-A): the regional distribution of the column load variations is well correlated with the DOD variations in Figure 8-A, which qualitatively confirms that the latter is nearly entirely due to the changed radiative feedback upon the dust mass. Under one possible feedback mechanism, the enhanced SW radiation reaching the surface (due to reduced absorption of the dust layer) increases boundary layer mixing and the vertical transport of strong winds aloft to the surface, thereby increasing dust emission (Miller et al., 2004; Pérez

375   et al., 2006). This dependence is consistent with the greater SSA and mass load in EXT with respect to the HOM control run. However, a fuller investigation of the complicated dependence of surface wind speed and atmospheric transport upon the dust DRE is beyond the scope of this paper.

The contrast of annual SSA due to varying mineralogy (Figure 8-B), according to the EXT coupling scheme compared to HOM, is remarkable in some locations. Among high-DOD regions, in northern Africa (including plumes over the Mediter-

380   ranean Sea), the Middle East and central Asia, we see positive SSA variations above 0.02 with peaks above 0.03 (e.g. in the northwestern Sahara), indicating a considerably higher scattering by dust in these regions. In contrast, we see smaller SSA variations (between 0.01 and 0.02) in the Arabian Peninsula and Australia, and almost negligible SSA variations ($< 0.01$) in the Sahel (and downwind over the Atlantic Ocean) and northern India. These regional variations reflect the distribution of the mineral components in the EXT experiment, that carry different absorption properties. The host mixture, with a much more

385   reflective (lower) IRI than our default dust IRI (Table B1), is the most abundant of the three components over most dust regions (Figure 10-C). The static accretion, whose IRI is higher than our default IRI at most wavelengths, is particularly abundant in the Sahel (Figure 10-D), due to the strong emission of iron oxides in this area (Claquin et al., 1999; Gonçalves Ageitos et al., 2023), where the SSA remains almost unchanged compared to the control experiment. This indicates that the effective absorption of a more abundant static accretion externally mixed with the background host amalgam resembles that of our default

390   homogeneous dust. Free iron oxides have a comparatively negligible influence upon SSA due to their irrelevant optical depth (Figure 10-B: note the different color scale).

As previously mentioned, overall dust becomes more scattering in the EXT experiment compared to the control run. It is important to point out that, while the emphasized regional differences in SSA are a direct consequence of the varying mineral composition, the general increase of dust scattering is relative to the specific IRI that we use for default dust in the control run

395   (Sinyuk et al., 2003). The latter is just one of the possible IRI sets for dust available in literature, but is the most reflective option implemented in ModelE2.1, and in general is less absorbing than other widely used prescriptions (e.g. Patterson et al., 1977; Hess et al., 1998). On the other hand, according to the soil map of Claquin et al. (1999), along with our optical modeling based on DB19 and SZ15, dust aerosols are mainly composed by weakly absorbing host minerals in most regions, and the effect
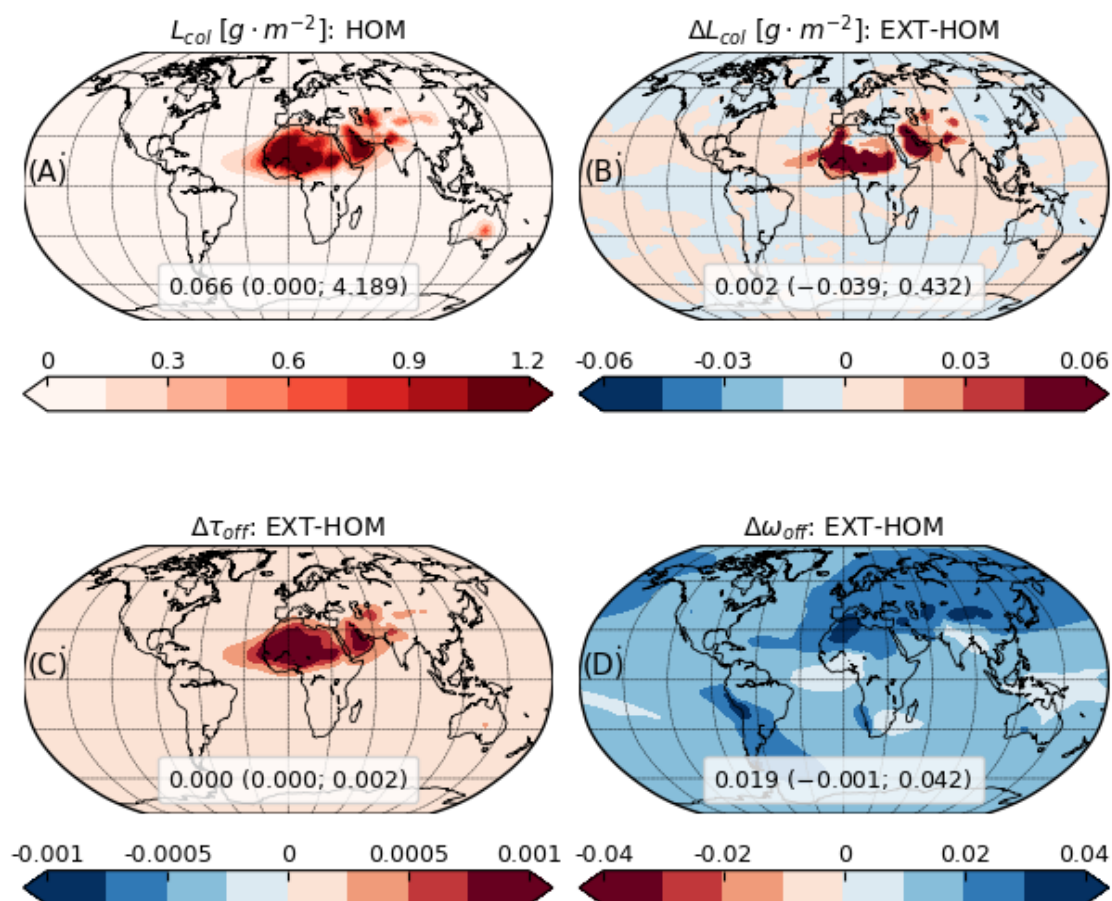
**Figure 9.** Top panels: annual mean column mass load ($L_{col}$) from the control run with homogeneous composition (HOM; A) and contrast between the mineral experiment with external mixing configuration (EXT) and HOM (B). Bottom panels: contrasts of annual mean dust optical depth ($\tau$; C) and single scattering albedo ($\omega$; D) of EXT with respect to HOM, calculated offline ($off$) by using the mass concentration of the three mineral components from HOM (in both cases) but distinguishing their refractive index in EXT. This calculation allows isolating the effect of a changed absorption from the contribution of a changed mass upon the optical properties. The optical properties are averaged over the spectral band of ModelE2.1 covering ultra-violet and visible wavelengths ($0.30 - 0.77\,\mu m$). The extremes of the color bars are set to include $1^{st}$ and $99^{th}$ percentiles of the mapped variables. Global average along with minimum and maximum (within parentheses) are also reported.
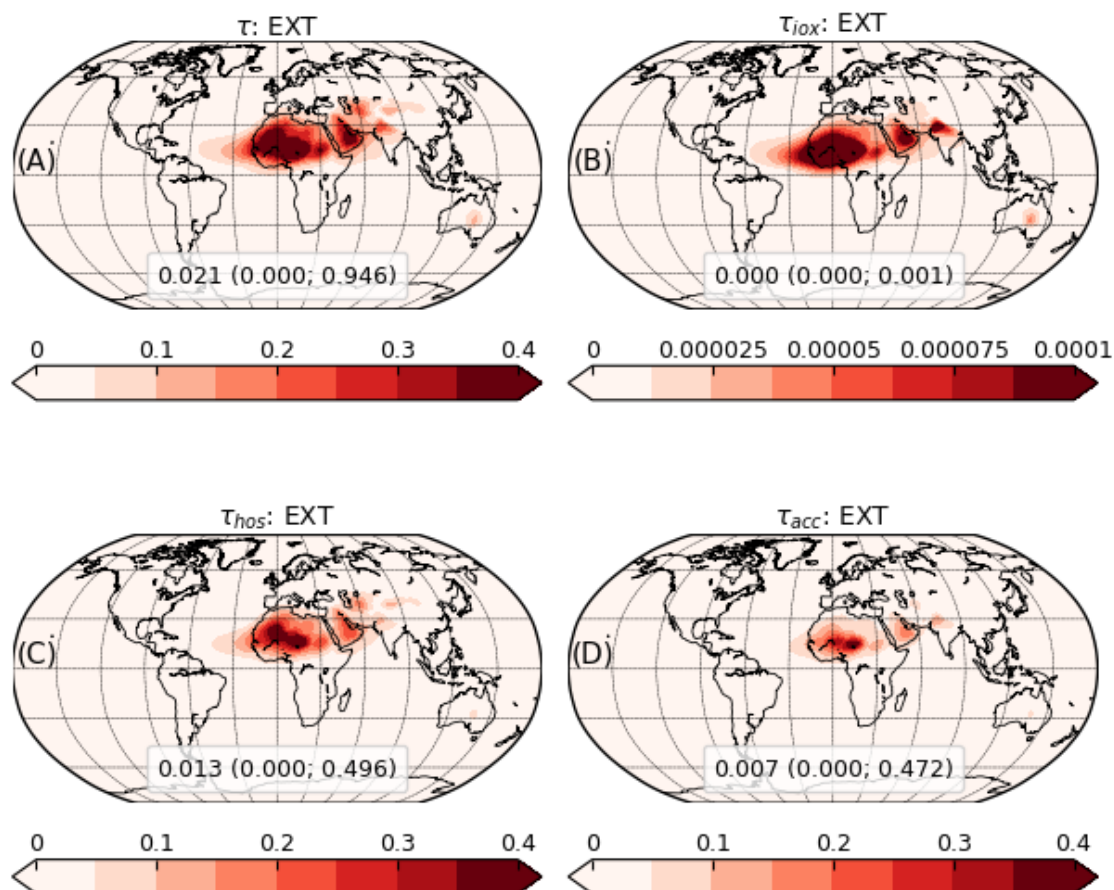
**Figure 10.** Annual mean dust optical depth ($\tau$) from the mineral experiment with external mixing configuration (EXT; A), decomposed into free iron oxides ($iox$; B), host amalgam ($hos$; C) and static accretion ($acc$; D). The optical depth is averaged over the spectral band of ModelE2.1 covering ultra-violet and visible wavelengths ($0.30 - 0.77\,\mu m$). The extremes of the color bars are set to include $1^{st}$ and $99^{th}$ percentiles of the mapped variables. Global average along with minimum and maximum (within parentheses) are also reported.

of absorbing iron oxides becomes relevant only in specific regions. The increase of dust scattering in the mineral experiment,
therefore, can be interpreted as follows: currently available information about relative abundances and optical properties of
minerals results in a less absorbing dust compared to existing prescriptions for unspeciated dust, even those that have been
traditionally considered highly reflective.

The negative contrast of annual DRE at TOA over most dust regions (Figure 8-C) is mainly determined by the increase of
SSA in the EXT experiment, and strengthened by the induced DOD increase. Over bright surfaces of prolific source regions
(e.g. the Sahara and southern Arabian Peninsula), where the default DRE is mostly positive (Figure 6-C), we see a strong
warming reduction due to the higher SSA that causes lower absorption by the dust layer and thus more radiation reflected back
to space. The negative DRE variations in these regions are quite uniform and large enough ($\gtrsim 0.75\,W \cdot m^{-2}$ in absolute value,
in most areas) to modify the sign of the DRE by default dust in specific areas (compare Figures 6-C and S1-A). Globally, the
mineralogy effect of the three externally mixed components produces an additional cooling at the TOA of $-0.047\,W \cdot m^{-2}$.
We roughly estimate a relative contribution of $\sim 81\,\%$ of the SSA variations to this additional cooling, by adjusting the DRE
in the HOM control run to the DOD of the EXT experiment.

In Figure 8-D, the enhanced SSA tends to reduce the cooling at SFC, because lower absorption leads to more forward-
scattered radiation. This effect is opposed by the induced DOD increases, which actually cause greater cooling where the SSA
contrast between the two experiments is comparatively small (e.g. in the Sahel). Globally, the externally mixed mineralogy
effect produces a reduction of cooling at SFC of $0.054\,W \cdot m^{-2}$.

### 3.1.3  Impact of mixing configuration for minerals (INT versus EXT)

In Figure 11, we evaluate the changes to DOD and SSA in the UV-VIS band, and the all-sky DRE at TOA and at SFC for the
entire SW spectrum, due to the assumed mixing configuration for minerals: INT (size-resolved internal mixing of all minerals)
with respect to EXT (external mixing of three mineral components). The SSA is larger in the INT experiment (indicating more
scattering), but the local contrast is small almost everywhere ($< 0.0075$; Figure 11-B) and the global mean contrast is only
0.006 (from 0.936 to 0.942; Table 3). This means that distributing iron oxides within a single mineral mixture, instead of
incorporating them with a fixed proportion within only a fraction of the host minerals, slightly reduces dust absorption but does
not substantially change the regional distribution of SSA. The SSA contrast between the two experiments is smallest downwind
of source regions with high soil fractions of iron oxides, such as Sahel sources to the west of Bodélé Depression as well as the
Kalahari Desert, where the fractional abundance of accretions is largest (Figure 15e of Perlwitz et al., 2015a). This suggests
that our two mixing configurations result in similar absorption when the simulated fraction of iron oxides is large enough to
substantially increase the IRI of the dynamic accretion (INT), according to Figure 3, so that the latter resembles the external
mixture of static accretion and the host amalgam in term of absorptive power. (Note that the IRI of static accretion is always
relative to a $5\,\%$ of iron oxides by mass.)

The increased SSA determines a further widespread negative contrast of the DRE at TOA over most dust regions (Figure
11-C), which is stronger where DOD increases are larger (Figure 11-A). The DRE variations are slightly lower in intensity
compared to that generated by EXT versus HOM, with a ratio of global mean contrasts of $74\,\%$, but are still able to modify the
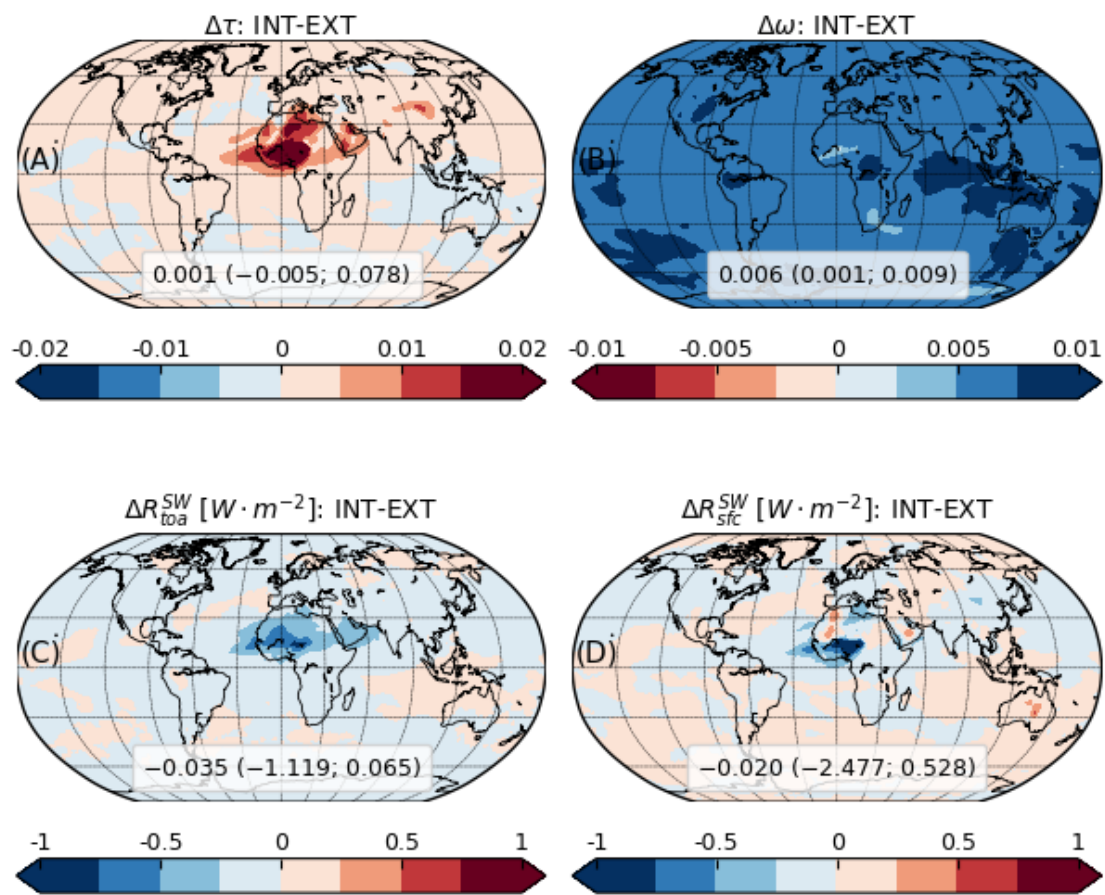
**Figure 11.** Same as Figure 6 but showing the contrast between the mineral experiments with internal (INT) and external (EXT) mixing configuration. Note that the color mapping for single scattering albedo indicates increased/decreased scattering with blue/red.

distribution of the DRE at TOA in specific areas (compare Figures S1-A and S1-B). Globally, configuring the minerals as one dynamic internal mixture (INT) generates an additional cooling of $-0.035\,W \cdot m^{-2}$ compared to the configuration with three externally mixed components (EXT). This is again mainly determined by the increased SSA ($\sim 64\%$), although the global mean DOD contrast ($+4.2\%$) makes a more relevant contribution than in EXT versus HOM.

At SFC (Figure 11-D), we see again the contrasting effect of SSA and DOD variations: while the SSA increase tends to reduce the cooling, the induced DOD increases soften this reduction and actually lead to cooling increases where they are relatively intense (e.g. plumes from the Sahel, over the Atlantic and the Mediterranean Sea). Globally, the INT scheme produces a cooling increase at SFC of $-0.020\,W \cdot m^{-2}$ with respect to EXT, which is primarily due to the enhanced DOD.

## 3.2 Comparison between model and AERONET dust optical properties

In Figures 12, 13 and 14, we compare monthly means of model dust SSA and DOD to the same variables retrieved for dusty scenes at the selected AERONET stations and months. Both model and AERONET optical properties are spectrally averaged over the UV-VIS band of ModelE2.1 ($0.30 - 0.77\,\mu m$). We compare SSA to data from the AeroTAU4 subset of stations while for DOD we use AeroTAU0: these data sets are defined based on the assumed minimum threshold for the AOD at $0.440\,\mu m$, as explained in Section 2.3. In Figure 12, we quantify the dispersion of SSA across stations and months through the standard deviation of the monthly means. Similarly, in Figures 13 and 14, we represent the variability of monthly SSA and DOD within each region and season through medians (solid bars) along with $1^{st}$ and $99^{th}$ percentiles (error bars). For clarity, in this analysis we refer always to Northern Hemisphere seasons.

### 3.2.1 Spatio-temporal correlation of monthly single scattering albedo

In Figure 12-A, we see that model SSA of homogeneous dust underestimates AERONET values in most regions and seasons. Our model simulates higher column volume fractions in the two coarsest bins ($8 - 32\,\mu m$ in diameter) than in AERONET (Figure S3). However, the AERONET volume size distribution is retrieved under certain assumptions (e.g. it must go to zero for diameters approaching $30\,\mu m$) and thus potentially underrepresents very large particles that may be present in the column (especially close to source areas). In this case, the missing absorption by coarse particles would be compensated by a higher retrieved IRI to preserve the SSA that allows the best fit to the measured sky radiances. On the other hand, as discussed in Section 3.1.1, our mass load in both fine ($0.1 - 5\,\mu m$) and coarse ($5 - 20\,\mu m$) diameter ranges results in good agreement with observational constraints (Adebiyi and Kok, 2020). These considerations suggest that the model underestimate of AERONET SSA in Figure 12-A is likely attributable to excessive dust absorption resulting from our specific prescription of globally uniform dust IRI from Sinyuk et al. (2003). Exceptions to this underestimate for some spring and summer months in North India may be partly due to contamination of our dusty AERONET scenes by absorbing carbonaceous species (Go et al., 2022).

In addition, our globally homogeneous dust produces a variability range of SSA across stations and months, attributable only to size variations, that is lower than the AERONET range: model and retrieved standard deviations are $\sigma = 0.006$ and $\sigma = 0.011$, respectively. Except for some SSA values above $\sim 0.92$ at northwestern African stations, such as Capo_Verde and
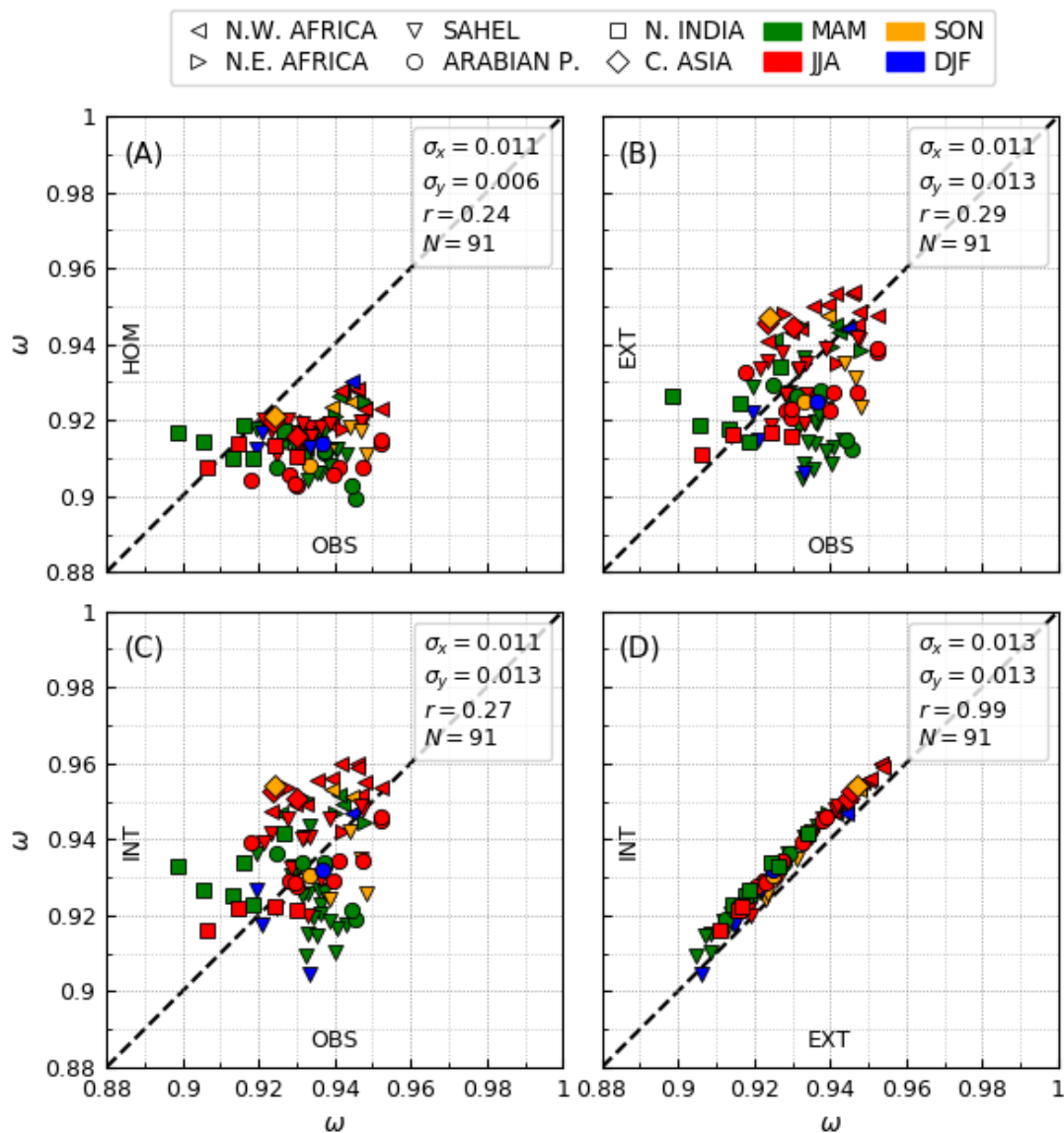
**Figure 12.** Monthly mean single scattering albedo ($\omega$) from model experiments compared to AERONET retrievals at the selected stations and months, labeled by region (Figure 5) and season (Northern Hemisphere spring: MAM, summer: JJA, autumn: SON, winter: DJF). The single scattering albedo is averaged over the spectral band of ModelE2.1 covering ultra-violet and visible wavelengths ($0.30 - 0.77\,\mu m$). AERONET monthly means (OBS) are separately compared to the control run with homogeneous composition (HOM; A), and the mineral experiments with external (EXT; B) and internal (INT; C) mixing configuration; the two mineral experiments are also directly compared (D). Standard deviation of the monthly means ($\sigma$), Pearson correlation coefficient ($r$) and number of monthly values ($N$) are also reported.

the sites in the Canary Islands (Figures 5 and 6-B), the model SSA ranges between $\sim 0.90$ and $\sim 0.92$, while AERONET SSA ranges from $\sim 0.90$ to $\sim 0.95$. The SSA variability is in general attributable to variations in size distribution, internal composition and particle morphology. A model PSD underrepresenting the real size variability, for example, may contribute to the mismatch between model and observed SSA ranges. However, our analysis suggests that part of the SSA range from
470  AERONET missed by the model may be explained by variations in mineralogy.

In Figures 12-B and 12-C, we show the model SSA in the EXT and INT experiments, respectively, compared to AERONET SSA. The first evident result is that accounting for varying mineral composition increases the model SSA values (which corresponds to greater scattering) and enlarges the SSA range, improving overall the agreement with the observed SSA. The EXT scheme produces SSA values between $\sim 0.91$ and $\sim 0.95$ and the same SSA dispersion of the INT scheme ($\sigma = 0.013$),
475  the latter reaching slightly higher SSA (up to $\sim 0.96$) except for some spring and winter months in the Sahel (consistent with Figure 11-B). This is more clearly visible in Figure 12-D, where we directly compare the EXT and INT experiments: only in one winter month is the SSA slightly lower in INT compared to EXT. This corroborates our argument (mentioned in Section 3.1.3): if the fraction of iron oxides becomes large enough, the INT configuration with dynamic accretion results in similar (or higher) absorption compared to the EXT configuration where the static accretion is externally mixed with the host mixture.
480  This SSA comparison demonstrates that prescribing a globally uniform IRI for dust, as most climate models still do, makes it challenging to reproduce the spatio-temporal variability of the observed dust SSA and inevitably generates biases across different regions, even if the chosen IRI is suitable for specific regions. In addition, consideration of mineral composition, regardless of our chosen mixing configuration, leads to better reproduction of the distribution of AERONET dust absorption across different locations and months, which suggests that the mismatch between ranges of model and observed SSA is actually
485  due to the effect of varying mineral composition. Finally, the model-AERONET correlation improves only very slightly in the mineral experiments (from $r = 0.24$ in HOM to $r = 0.29$ and $r = 0.27$ in EXT and INT, respectively): this increase calculated for $N = 91$ values is not statistically significant according to a two-sided $95\,\%$ confidence interval. In any case, the moderate correlations in the mineral experiments suggest remaining model limitations in correctly simulating the mineral composition of dust aerosol and its absorption properties (see Section 4).

490  **3.2.2  Regional and seasonal comparison of monthly single scattering albedo and optical depth**

The regional-seasonal SSA comparison, in Figure 13, corroborates our interpretation of Figure 12. Almost everywhere and in all seasons, AERONET SSA is higher than the SSA of the default dust model (HOM) and shows larger variability across different regions, with individual station values from $\sim 0.90$ in North India in spring months to peaks exceeding $0.95$ in the Arabian Peninsula in summer months. In contrast, the default model SSA ranges from $\sim 0.90$ to $\sim 0.93$ at AERONET sites,
495  consistent with Figures 6-B and 12-A. Also the inter- and intra-seasonal SSA variability within each region is generally higher in AERONET than in our HOM experiment in most regions: e.g. note the remarkable drop of observed SSA from autumn to winter in the Sahel that is absent in the HOM experiment, or the larger AERONET error bars in northeastern Africa, the Sahel during summer and winter, Arabian Peninsula during summer and northern India.
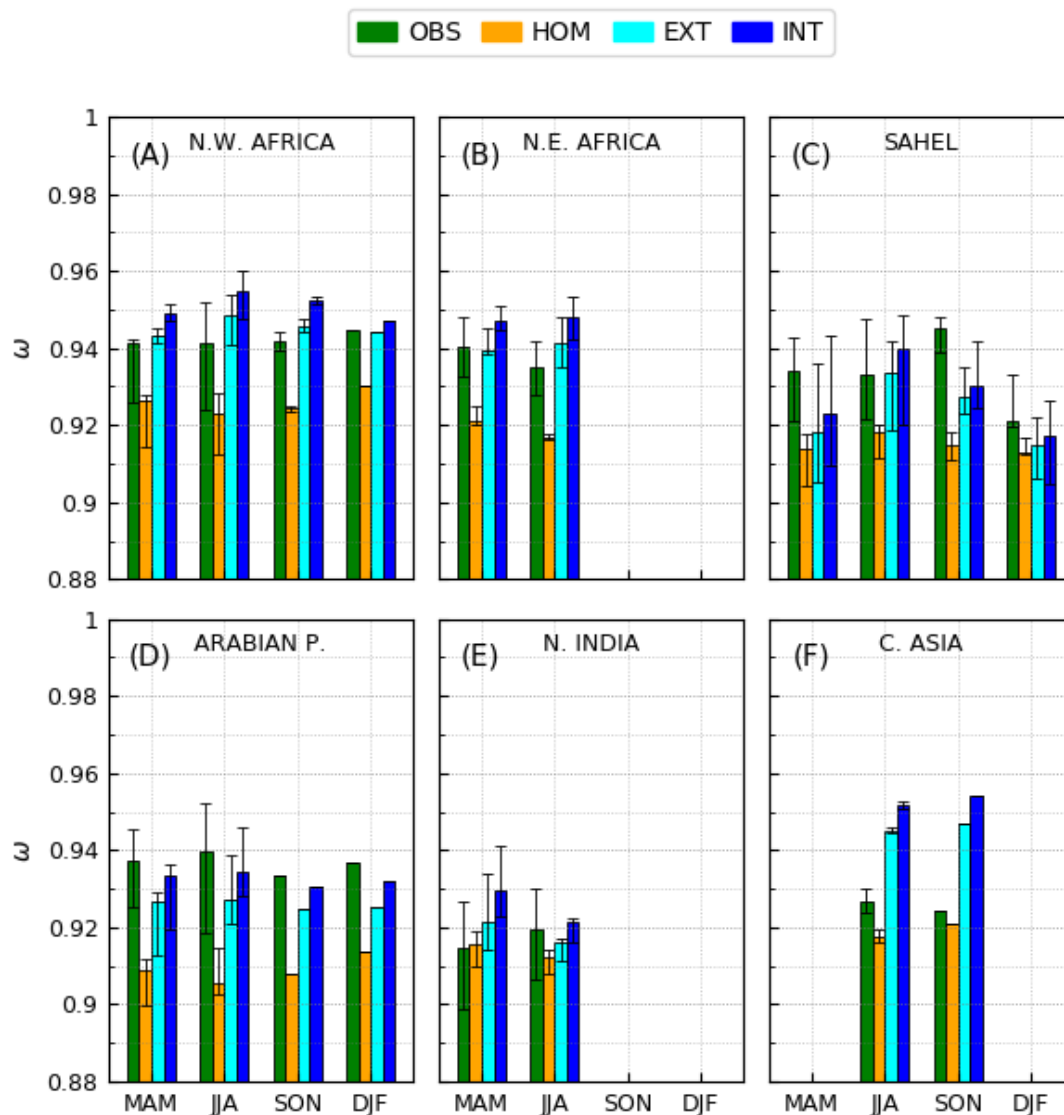
**Figure 13.** Monthly mean single scattering albedo ($\omega$) from the control run with homogeneous composition (HOM), and the mineral experiments with external (EXT) and internal (INT) mixing configuration, compared to AERONET monthly retrievals (OBS) at the selected stations and months, grouped per region (Figure 5) and season (Northern Hemisphere spring: MAM, summer: JJA, autumn: SON, winter: DJF). The single scattering albedo is averaged over the spectral band of ModelE2.1 covering ultra-violet and visible wavelengths ($0.30 - 0.77 \, \mu m$). The solid bars represent medians, along with $1^{st}$ and $99^{th}$ percentiles (error bars), of the monthly means within each region and season.

The evaluation is improved by representing spatial and temporal variations of dust mineral composition, which first of all
500    generates a higher model SSA, with INT values consistently higher than EXT values (as already seen in Figures 11-B and 12-
D). Note that in the Sahel during winter both the EXT and INT experiments reproduce the wintertime increase in absorption
indicated by AERONET, in contrast to the HOM experiment. The varying mineralogy effect also generates larger regional
and seasonal SSA variability, and thus generally improves the agreement with AERONET observations. However, evident
discrepancies between coupled models and AERONET SSA remain; one example is the model SSA of mineral experiments
505    tending to overestimate the AERONET values in northern Africa and underestimate them in the Sahel in most seasons (see
Section 4.1 for more details about this result). Evaluation of the annual cycle does not present a clear conclusion: the model
simulates slightly more scattering dust during summer in northern Africa and the Sahel, but this tendency is less clear for the
AERONET observations, whose annual cycle is different for each region.

AERONET DOD is underestimated by the model in most regions and seasons (Figure 14), which is consistent with our
510    global DOD underestimating the observational constraint provided by Ridley et al. (2016), although we find good agreement
in the Sahel and Arabian Peninsula, possibly due to a better modeled emission in these source regions. Despite the partial
mismatch of values, we highlight the good agreement between model and observed annual cycles: the observed DOD peaking
during summer or spring, before going down in autumn and winter, is generally well reproduced by the model. DOD differences
resulting from different model optical configurations are not as important as for SSA. We see small DOD contrasts due to a
515    differing radiative feedback upon dust emission and mass load (Figures 8-A and 11-A).

## 4   Sources of uncertainty

### 4.1   Inaccuracy of soil mineralogy map and model processes

Soil fractions of the eight minerals simulated here are characterized by only a couple hundred measurements worldwide.
Claquin et al. (1999) circumvented this scarcity by characterizing soil mineral composition using comparatively abundant sur-
520    veys of soil type that are available globally, assuming that each type has a characteristic mineral content: the 'Mean Mineralogy'
assumption. The inferred mineral fractions are uncertain both because of the limited measurements available to establish the
composition of each soil type and the neglect of mineral variations within a single soil type across different regions. Journet
et al. (2014) revisited soil mineralogy, increasing the number of measurements and using the soil unit descriptor to extend the
mineral fractions to a global scale. Simulations using both representations of soil composition perform comparably, although
525    the evaluation is limited by the sparsity of atmospheric measurements of aerosol mineralogy (Gonçalves Ageitos et al., 2023).
The soil fractions of some radiatively important minerals like iron oxides are additionally uncertain due to qualitative met-
rics that describe their abundance, like the 'redness' of the soil. All these challenges are currently being addressed through
spaceborne hyperspectral imaging from the International Space Station as part of NASA's Earth Surface Mineral Dust Source
Investigation (EMIT) that will provide billions of mineral identifications based on their spectral dependence across near-UV,
530    VIS and NIR wavelengths (Green et al., 2020). This project will be especially effective at detecting iron oxides like hematite
and goethite that have prominent absorption features in the UV and VIS bands.
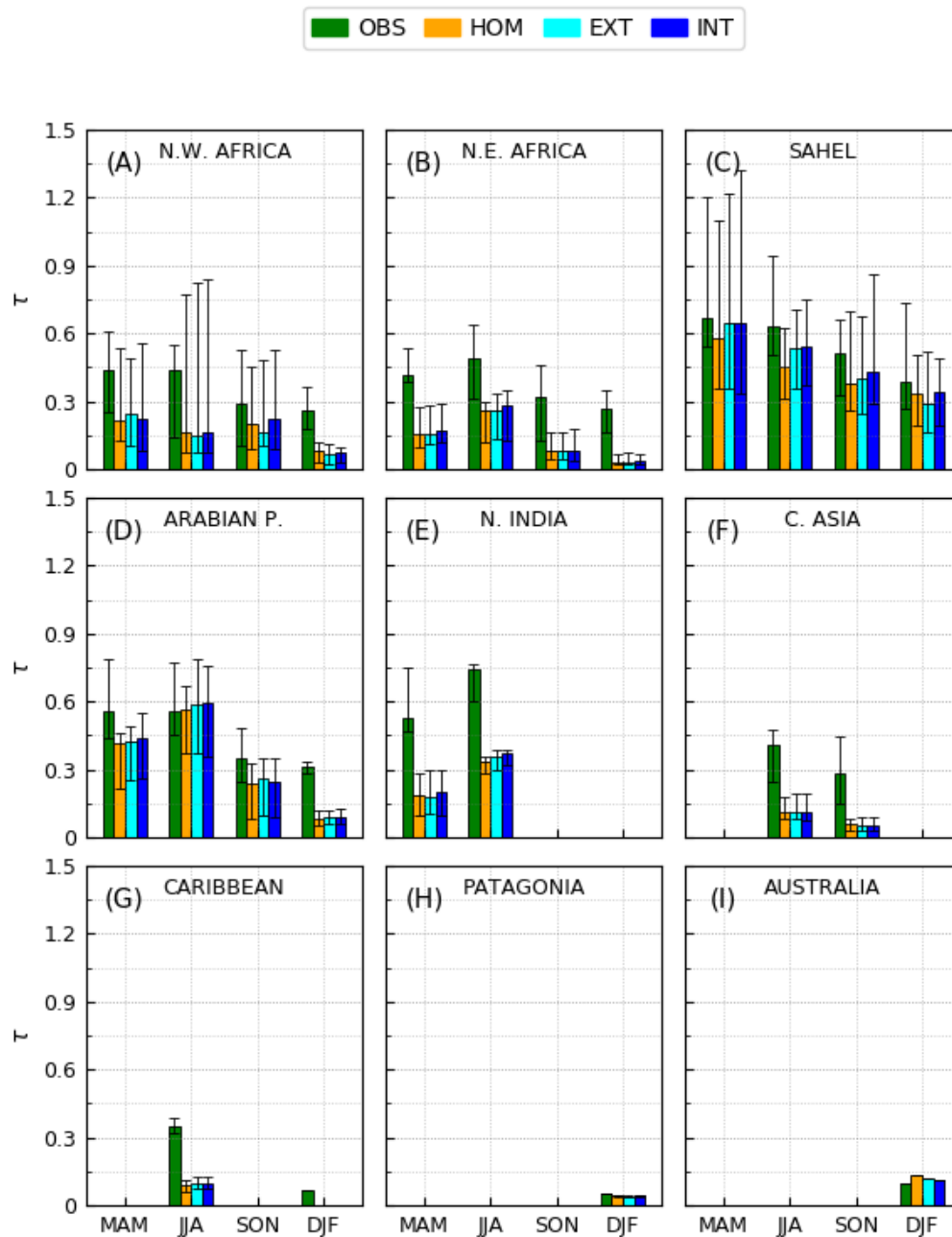
**Figure 14.** Same as Figure 13 but showing the comparison between model and AERONET dust optical depth ($\tau$).

Other model errors of mineralogy arise from the limited spatial resolution of the ESM. This is a special problem for emission, which depends upon the relation of dust sources to the local surface winds that are partly steered by topography that in the model may be smoothed. This leads to calculations of emission by different ESMs with varying regional emphases and biases (Kok et al., 2021). The model resolution also degrades the spatial detail of the soil unit and soil type atlases, blurring the mineral fractions. Additional modeling challenges are: the emitted PSD that is assumed to be globally uniform, except for small differences across the silt bins due to geographically varying mineral composition (Perlwitz et al., 2015a), possible transport errors that may cause plumes from different source regions to be mixed with biased proportions, and the possibly excessive removal of coarsest particles during transport resulting in underestimated coarse fractions far from sources (e.g. van der Does et al., 2016).

The aerosol mineral composition calculated by the model is influenced by all these uncertainties, that may lead to biased relative abundances of minerals and thus eventually impact the absorption properties of the dust mixture at specific grid boxes. For example, during spring, our mineral experiments calculate much lower SSA in the Sahel compared to northwestern Africa, whereas AERONET reports similar SSA (Figure 13). This contributes to the slightly excessive ranges and moderate correlations of model SSA compared to AERONET (Figures 12-B and 12-C). Our model contrast results from higher emitted fractions of iron oxides in the Sahel than in the Sahara (Figure 12 of Perlwitz et al., 2015a), which is consistent with the composition measurements by DB19 (except in the Bodélé depression). Given that AERONET photometers scan the entire column, part of the error could be inaccurate transport of model dust between these two regions in specific seasons that results in insufficient mixing of dust plumes carrying different absorption properties.

## 4.2 Uncertainty in optical modeling of minerals

A source of uncertainty in our optical modeling of minerals is the definition of a single globally uniform host mixture, whose CRI is calculated by composing host minerals and then averaging over the dust aerosol samples of DB19. This implies our neglect of absorption differences among host minerals, as collected by SZ15. For example, the IRI of illite and smectite is three orders of magnitude smaller than the IRI of iron oxides at UV-VIS wavelengths, but quartz and calcite absorb even less (Figure 2-B). This neglect is a helpful modeling simplification but may partially bias the regional distribution of model SSA, especially where concentrations of host minerals are high compared to those of iron oxides. For example, our model emits high fractions of clay-sized illite from the Sahara Desert, while within the Sahel the host minerals are dominated by phyllosilicate kaolinite (Figure 10 of Perlwitz et al., 2015a) which is less absorbing than illite (Figure 2-B): this contrast of absorption between the two minerals is neglected by our model.

Moreover, uncertainty in the IRI retrievals from DB19, as well as in our polynomial representation of their empirical relation to the iron oxide content (Figure 3), directly impacts our IRI calculation for accretions. For example, DB19 retrieved an 'effective' IRI in each dust aerosol sample (using the measured volume size distribution) that is representative of homogeneous spherical particles within a bulk size range up to $\sim 10\,\mu m$ in diameter. One uncertainty is that we use the same relation between IRI and iron oxides for each of our size bins, neglecting any possible size effects upon the inversion calculation. Our assumption is partially supported by DB19, as they reported a negligible dependence of the retrieved IRI upon the settling of

the coarser particles in each sample during the experiment duration ($2\,h$). This suggests that the resulting reduction of size range did not significantly affect the relation of the retrieved IRI to the unchanged fractional amount of iron oxides (measured by accumulating filtered aerosol mass for the entire experiment duration). However, a systematic validation would be useful to strengthen the use of the empirical relationships within different size ranges (also beyond $10\,\mu m$).

570    On the other side, errors of the AERONET retrievals may affect the comparison between model and observed SSA in Figures 12 and 13. We estimate an uncertainty of $\lesssim 0.007$ in the monthly SSA that results from measurement errors and uncertain auxiliary inputs in the original hourly SSA retrievals (Level 2.0), whose individual uncertainty is $\sim 0.03$ (Dubovik et al., 2002; Sinyuk et al., 2020). In contrast, an inaccurate selection of dusty scenes has a potential impact upon the observed SSA that we use in our analysis. Despite our strict conditions to isolate dust events, even a small contamination by residual carbonaceous

575    absorption (i.e. by BC and BrC) may still affect the observed SSA in specific stations and months (Schuster et al., 2016). This error, however, is difficult to characterize.

## 5    Conclusions

In this work, we couple spatially and temporally varying aerosol mineral composition, derived from regionally varying soil mineralogy (Claquin et al., 1999), to radiative fluxes in the NASA GISS ModelE2.1. In general, measurements of dust particle

580    morphology that might guide model representations of mineral mixtures are available only from limited field campaigns (e.g. Kandler et al., 2009; Panta et al., 2022). Deriving the particle CRI from the indices of the constituent minerals requires the application of approximate theoretical mixing rules, whose validity is difficult to assess, that are based on idealized spatial arrangements of minerals within dust particles. As an alternative approach, we link the dust absorption to mineral composition according to empirical relationships proposed by DB19 that relate dust IRI at solar wavelengths to the mass fraction of

585    iron oxides. We assess the effect of varying composition upon dust optical properties (DOD and SSA) in the UV-VIS band ($0.30-0.77\,\mu m$) and the DRE summed across the SW spectrum. To evaluate the sensitivity of our results to the mixing state of minerals, we use two alternative mineral-radiation coupling schemes. For the INT experiment, all minerals are blended into a size-resolved single internal mixture whose IRI is proportional to the spatially and temporally varying iron oxide mass fraction. In contrast, for the EXT experiment, we define a homogeneous amalgam of non-iron oxide minerals, based on aerosol volume

590    fractions from DB19 combined with CRIs of single minerals from SZ15, that we externally mix with another component comprised of this amalgam internally mixed with iron oxides. (A third component containing pure iron oxides makes a negligible contribution to the total DOD and SSA.) We evaluate the model SSA and DOD against observations from AERONET filtered for dust events. We define a new technique for selecting scenes dominated by dust in AERONET, based on filtering conditions applied to retrievals of size (FVF) and absorption properties (SSA and IRI) of both the dust and non-dust aerosol species at

595    solar wavelengths (see also Gonçalves Ageitos et al., 2023).

    In the HOM control experiment, assuming globally homogeneous composition, we use dust IRI retrieved in areas affected by Saharan dust sources (Sinyuk et al., 2003) that is typically taken by modelers as globally representative (Miller et al., 2006; Yoshioka et al., 2007). Our dust model, also in the mineral experiments, underestimates the mass extinction efficiency esti-

mated by Kok et al. (2017) based on a combination of satellite, in situ and modeling constraints, as we calculate a higher global

mass load and lower mean DOD. Given that the size distribution of our global mass load is consistent with the observationally

constrained distribution of Adebiyi and Kok (2020), we attribute this extinction bias to our simplistic assumption of spherical

particle shape. Kok et al. (2017) calculated that approximating the highly irregular shapes of natural dust particles (Kalash-

nikova and Sokolik, 2004; Huang et al., 2020) with tri-axial ellipsoids (Meng et al., 2010) leads to significantly larger extinction

efficiency, mostly due to the higher cross-sectional area of ellipsoids with respect to volume-equivalent spheres (Huang et al.,

2023). On the other hand, our use of Mie theory to compute optical properties (Appendix B) is consistent with the assumption

of spherical shape in the inversion calculation of dust IRI by DB19. While we address the shape effect upon optical properties

and DRE of unspeciated dust in an upcoming study, we need to assess its impact upon the retrieved empirical relations of

dust IRI to the fractional mass of iron oxides before extending our approach for coupling minerals to radiation by representing

non-spherical particles.

Compared to the control case, the mineral experiments generally exhibit higher scattering, with the SSA increasing from

0.917 in HOM to 0.936 and 0.942 in EXT and INT, respectively, and slightly higher DOD (from 0.020 in HOM to 0.021 and

0.022 in EXT and INT, respectively) due to the radiative feedback upon dust emission. The mineral-induced SSA contrasts

emphasize some regional differences, for example between the Sahara and the Sahel, that are mainly determined by the varying

abundance of iron oxides. Simulated iron oxide fractions result in similar absorption compared to our unspeciated default dust

(e.g. in the Sahel). The regional variations in SSA and DOD perturb the spatial distribution of DRE, both at TOA and at SFC,

with a potential impact upon regional climate. Globally, the increased SSA is the main contributor to larger cooling at TOA:

SW DRE varies from $-0.25$ in HOM to $-0.30$ and $-0.34\,W\cdot m^{-2}$ in EXT and INT, respectively. The SW effect is offset by

the positive LW DRE (Table 3), so that the net DRE is smaller: $-0.12$ and $-0.15\,W\cdot m^{-2}$ for the EXT and INT experiments,

respectively (see also Figures S2-A and S2-B), compared to $-0.08\,W\cdot m^{-2}$ for the HOM control run. The varying mineralogy

also leads to a weaker cooling at SFC with a SW DRE from $-1.03$ in HOM to $-0.97$ and $-0.99\,W\cdot m^{-2}$ in EXT and INT,

respectively. At SFC, INT results in stronger cooling than EXT, due to the greater effect of the increased DOD.

Dust optical properties and DRE are sensitive to the mixing state of minerals, with a consistent increase of both DOD and

SSA, along with a larger global cooling at TOA, when all minerals (including iron oxides) are amalgamated into a single

internal mixture (INT) compared to accreting iron oxides within only a fraction of the host minerals (EXT). Compared to the

HOM control run, the change to the SW DRE at TOA in INT ($-0.083\,W\cdot m^{-2}$) is nearly two times larger in magnitude than

in EXT ($-0.047\,W\cdot m^{-2}$).

The explicit accounting of aerosol mineral composition and its spatio-temporal variations increases the model SSA, reducing

its bias in comparison to AERONET observations, and also enlarges SSA variations across different stations and months,

further improving the agreement with AERONET. In contrast, assuming homogeneous composition, according to the specific

IRI from Sinyuk et al. (2003), results in excessive absorption with respect to AERONET SSA without reproducing the full

retrieval variability. The reduction in absorption bias associated with mineral variations originates from a combination of two

factors. First, aerosol absorption arises solely from the regionally varying fraction of iron oxides in the soil, being the other

simulated minerals comparatively weakly absorbing. In addition, in the soil mineralogy of Claquin et al. (1999), hematite is

assumed to be the sole iron oxide, even though it is often accompanied by goethite, another iron oxide that is more weakly
635     absorbing (Formenti et al., 2008; Bedidi and Cervelle, 1993). We indirectly account for the presence of goethite by choosing the
DB19 empirical relations between IRI and the mass fraction of both iron oxides, thus interpreting our actual hematite fraction
more generally as a less absorbing iron oxide mixture including goethite. Our results indicate that realistic representation of the
dust absorption at UV-VIS wavelengths must be founded upon accurate prescription of both hematite and goethite fractions in
soils, and separate modeling of their radiative effect. These improvements may also lead to stronger correlation between model
640     and AERONET SSA at specific locations and months, while keeping the agreement in the variability ranges.

Measurements to evaluate the modeled aerosol mineral fractions are limited (Perlwitz et al., 2015b; Pérez García-Pando
et al., 2016), which results in uncertain estimates of measurement climatologies. In contrast, modelers are on the verge of
greatly improved knowledge of soil mineral content from the NASA Earth Surface Mineral Dust Investigation (EMIT) hyper-
spectrometer that is currently measuring VIS and NIR radiances from the International Space Station. The few hundred soil
645     analyses that are the basis for current soil atlases like Claquin et al. (1999) and Journet et al. (2014) will be supplemented with
over a billion retrievals of soil minerals, providing knowledge of soil composition with both greater regional detail and global
extent (Green et al., 2020).

Despite the remaining discrepancies with respect to AERONET, this work represents a promising step towards a refined
modeling system capable of incorporating the huge amount of information about soil composition that will soon be provided
650     by EMIT. This could allow the NASA GISS ModelE2.1 to achieve a more realistic representation of dust as a composite of
different minerals that would enable an improved assessment of the dust DRE and its impacts upon regional and global climate.

## Appendix A: Derivation of the imaginary index of free iron oxides

In the EXT scheme, we need to assign a CRI to the radiatively active component consisting solely of crystalline or free iron oxides. Here, we describe the inversion procedure to calculate the IRI of iron oxides consistent with the empirical relationships of DB19, that we compare to literature values corresponding to iron oxide minerals like hematite and goethite (Figure 4). As a first step, we must assume a mixing rule that links the IRI of dust particles to that of its constituent minerals. Figure A1 shows that commonly used mixing rules such as VM (volume-weighted mean), MG (Maxwell Garnett) and BG (Bruggeman) are approximately linear for small fractions of iron oxides (as measured by DB19). (VM is exactly linear for any amount of iron oxides.) This linearity suggests that we can derive the IRI of iron oxides by matching an analytic expression of a mixing rule (that we derive below) to the linear regression of the empirical relationships from DB19 between the particle IRI and the iron oxide fraction.

In general, the MG mixing rule (Markel, 2016) gives the effective complex permittivity $\epsilon = (n + ik)^2$, where $n$ and $k$ are the RRI and IRI, respectively, of a composite (in our case: accretion) starting from the permittivities of a homogeneous host medium and small inclusions (iron oxides). In the linear limit for small volume fractions of iron oxides ($v_{iox}$), the MG expression is identical to BG (Markel, 2016) and given by:

$$\begin{cases} \epsilon_{acc} & = \epsilon_{hos} + 3\epsilon_{hos}Xv_{iox} \\ X & = \frac{\epsilon_{iox}-\epsilon_{hos}}{\epsilon_{iox}+2\epsilon_{hos}}, \end{cases} \tag{A1}$$

whose imaginary component is:

$$2n_{acc}k_{acc} = 2n_{hos}k_{hos} + 3Iv_{iox}, \tag{A2}$$

where the factor $I$ is the imaginary part of the product $\epsilon_{hos}X$. From Equation A2, it is evident that MG couples the RRI and IRI of the accretion, which in turn depend upon coupled RRIs and IRIs of both the host medium and iron oxides according to a non-linear relation. Therefore, to derive an equation only for IRIs, an independent constraint upon the RRIs is required. For simplicity, we use Equation 2 as the linear relation among the RRIs of accretion, host medium and iron oxides: as already discussed in Section 2.2.3, for small fractions of iron oxides, different mixing rules result in negligible differences in accretion RRI. Substituting Equation 2 into Equation A2 leads to:

$$k_{acc} = \frac{n_{hos}k_0 + (3/2)Iv_{iox}}{n_{hos} + (n_{iox} - n_{hos})v_{iox}}, \tag{A3}$$

where we indicate the host medium IRI with $k_0$ to highlight that here it is in general different from the IRI of the host amalgam calculated in Section 2.2.2 ($k_{hos}$ of Equation 1), as it takes value from the linear regression of the empirical relationships of DB19 (see below). Expanding Equation A3 to the first-order term in the volume fraction of iron oxides results in the final analytic expression of the accretion IRI:

$$k_{acc} = k_0 + \frac{(3/2)I - k_0(n_{iox} - n_{hos})}{n_{hos}}v_{iox} = k_0 + l_1 v_{iox}. \tag{A4}$$
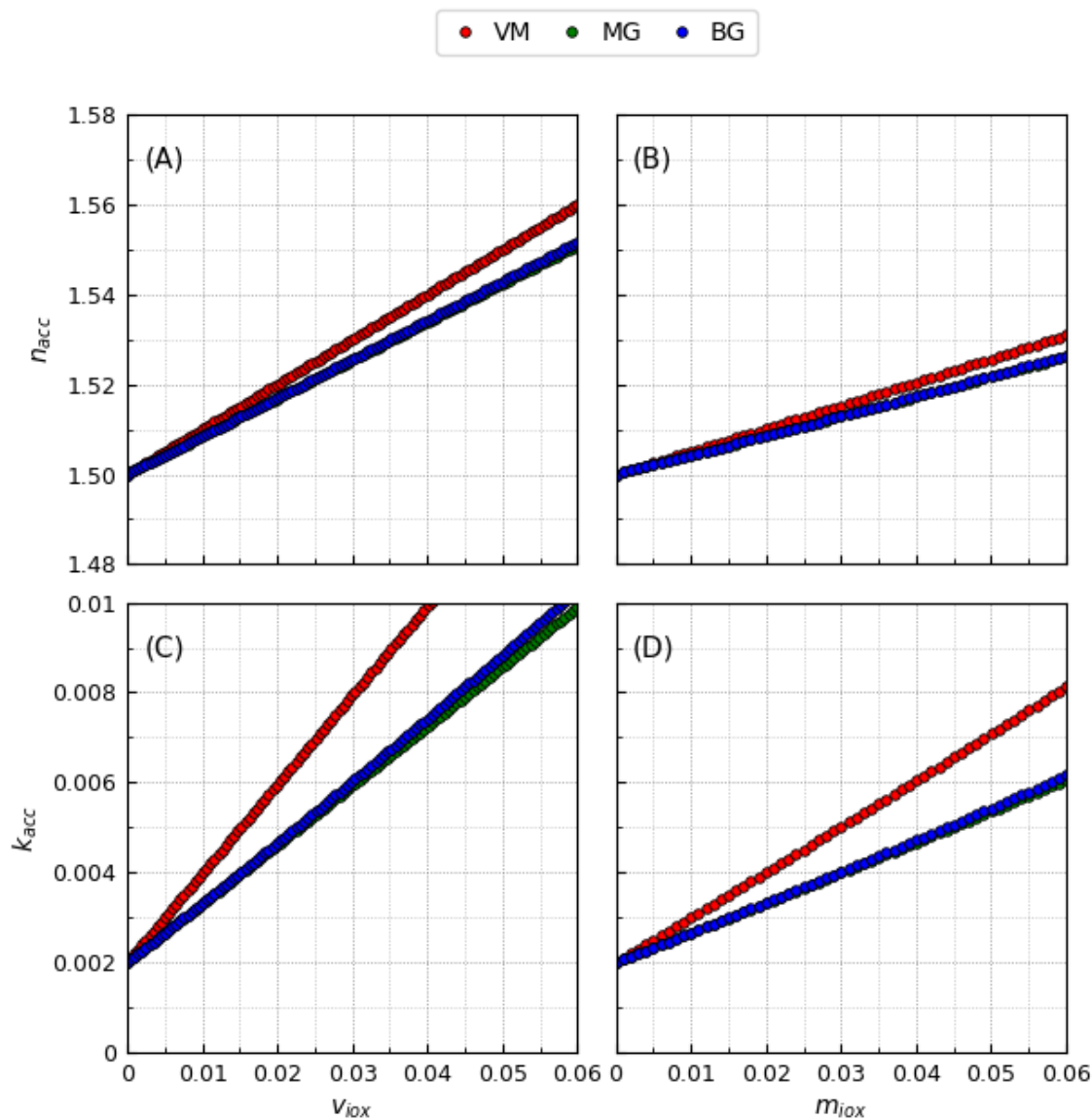
**Figure A1.** Test calculation of the dependence of real ($n_{acc}$) and imaginary ($k_{acc}$) indices of an accretion-like composite particle upon the volume ($v_{iox}$) and mass ($m_{iox}$) fractions of an iron oxide-like inclusion embedded in a homogeneous host-like medium, according to different mixing rules (volume-weighted mean: VM; Maxwell Garnett: MG; Bruggeman: BG) in the limit of small fractions of the inclusion ($< 0.06$). The real indices of inclusion and host are set to $n_{iox} = 2.5$ and $n_{hos} = 1.5$; the imaginary indices to $k_{iox} = 0.2$ and $k_{hos} = 0.002$; the mass densities to $\rho_{iox} = 5\,g \cdot cm^{-3}$ and $\rho_{hos} = 2.5\,g \cdot cm^{-3}$.

We assume now that dust particles of DB19 are two-component accretions whose IRI follows the linearized MG rule given by Equation A4, that we directly match to a linear regression of DB19 data to estimate the IRI of iron oxides. Given the non-trivial expression of the factor $I$ in Equation A4 (i.e. Equations A1 and A2), we apply an inversion procedure consisting of the following steps:

685    1. We perform a linear regression of the IRI retrievals of DB19, for all measurement wavelengths, with respect to the volume fractions of iron oxides in their dust aerosol samples, which we derive from the mass fractions using the mineral mass densities in Table 1; we thus estimate the empirical fit intercept ($l_0^*$) and slope ($l_1^*$).

   2. We calculate the factor $I$ for a high number of input IRI of iron oxides, and then the analytical slope ($l_1$) in Equation A4 using the known RRIs of the host amalgam (Section 2.2.2) and iron oxides (taken from SZ15), and the empirical intercept as the host medium IRI: $k_0 = l_0^*$; we span ten-thousand logarithmically equidistant IRI values between $0.001$ and $1$ for iron oxides, resulting in a relative accuracy of $\sim 0.07\%$.

   3. We infer the IRI of iron oxides by selecting the input value that makes the analytical and empirical slopes equal: $l_1 = l_1^*$; we also derive the uncertainty on the inferred IRI by perturbing the empirical slope based on the fit error (varying the empirical intercept has negligible impact).

695 Figure 4 shows our calculated IRI of iron oxides at VIS wavelengths, that is roughly intermediate between the IRIs for pure hematite and goethite measured by Bedidi and Cervelle (1993).

This derivation contains an inconsistency compared to our assumptions elsewhere in this work. The linear regression of the IRI retrievals from DB19, along with the unconstrained fit intercept used for the host medium, differ from the polynomial representation of Figure 3. For calculating the IRI of accretions (Section 2.2.3), we choose the polynomial function to reduce 700 the systematic low bias of the linear function resulting for large mass fractions of iron oxides while the host amalgam (Section 2.2.2) is set in the limit of vanishing iron oxides. This suggests that the candidate mixing rules of Figure A1 are not suitable for our IRI calculations for accretions and host mixture consistent with DB19 and SZ15. Nonetheless, deriving a mixing rule that diverges from linearity for small volume fractions of iron oxides while being consistent with Maxwell's Equations is outside of the scope of this work. In any case, this inconsistency has little practical impact given the small radiative effect of pure iron 705 oxides in our model calculations (Figure 10), but could be addressed in future studies.

## Appendix B: Calculation of dust optical properties

In this section, we describe the calculation of dust optical properties within the discrete SW bands of ModelE2.1 that we use in our experiments, including the HOM control run in which we assume globally homogeneous composition, and the EXT and INT experiments in which instead we implement a dependency upon the varying mineral composition.

### B1 Sets of complex refractive index

Given the CRIs for the mineral components at the seven wavelengths of DB19 (Sections 2.2.2 and 2.2.3, and Appendix A), to improve the accuracy of our optical calculations, we extrapolate the CRIs to twenty wavelengths ranging from 0.30 to $1\,\mu m$ which are a sub-set covering the UV-VIS band $(0.30 - 0.77\,\mu m)$ from the full-set of SW wavelengths at which the default dust CRI is prescribed in ModelE2.1 (Table B1). (The remaining five NIR bands cover wavelengths from $0.77$ to $4\,\mu m$.) We use spline interpolation to spectrally extend the CRIs of host mixture and iron oxides, as well as the fitting polynomial function, and then calculate the CRI for static and dynamic accretions using Equations 1 and 2 (Table B1).

### B2 Optical properties for default dust

We pre-calculate offline the optical properties of default dust used by the SW radiation scheme of ModelE2.1, which are the extinction and scattering efficiencies, along with the asymmetry parameter. First, we calculate mono-disperse optical properties for spherical particles using the Mie code from Mishchenko et al. (2002), as functions of the default CRI (Table B1) that is globally uniform but varies across wavelengths, and the size parameter that is defined as $x = \frac{\pi d}{\lambda}$, where $d$ is the particle diameter and $\lambda$ the wavelength. We consider a size parameter grid of five-thousand values ranging from $0.02$ to $1000$ with constant logarithmic steps. Next, we integrate the mono-disperse optical properties over each aerosol size bin for the full-set of default SW wavelengths (up to $4.114\,\mu m$; Table B1). For size integration, we use a step number distribution ($f_N$) corresponding to a constant volume size distribution on logarithmic scale within each bin, and zero outside (Tegen and Fung, 1994):

$$f_N(d) = \begin{cases} Cd^{-4} & \text{for } d \in (d_A, d_B) \\ 0 & \text{for } d \notin (d_A, d_B) \end{cases} \tag{B1}$$

where $C$ is a normalization constant and $(d_A, d_B)$ are the prescribed diameter bounds of the size bins reported in Table B2 (Perlwitz et al., 2015a). Equation B1 is used also to calculate the effective diameter (double of mean radius over the cross-sectional area distribution) corresponding to each bin (Table B2). The size-integrated single-wavelength optical properties are mapped onto a $10\,nm$-resolution wavelength grid and then averaged over the six SW bands, weighted by the solar flux (Thekaekara, 1974).

### B3 Optical properties for mineral components

The optical properties for mineral components are calculated during runtime only in the UV-VIS band of ModelE2.1 $(0.30 - 0.77\,\mu m)$. After defining the CRI for each mineral component (Table B1), either globally uniform for free iron oxides, host

**Table B1.** Real and imaginary refractive indices ($n + ik$), for the sub-set of twenty default shortwave wavelengths ($\lambda$), used in this work for: default dust ($hom$) in the control run with homogeneous composition (HOM) (Sinyuk et al., 2003; Volz, 1973); free crystalline iron oxides ($iox$), host amalgam ($hos$) and static accretion ($acc$) in the mineral experiment with external mixing configuration (EXT) (Di Biagio et al., 2019; Scanza et al., 2015). The best fit parameter defining the polynomial fitting function ($p_1$ in Equation 1), that is also used in the mineral experiment with internal mixing configuration (INT), and the CRI of default dust for the full-set of shortwave wavelengths up to $4.114\,\mu m$ are also reported.

| $\lambda\,[\mu m]$ | $n_{hom} + ik_{hom}$ | $n_{iox} + ik_{iox}$ | $n_{hos} + ik_{hos}$ | $n_{acc} + ik_{acc}$ | $p_1$ |
|---|---|---|---|---|---|
| 0.300 | $1.600 + i8.700\cdot10^{-3}$ | $1.682 + i2.871\cdot10^{-2}$ | $1.531 + i1.352\cdot10^{-3}$ | $1.535 + i6.832\cdot10^{-3}$ | $3.444\cdot10^{+1}$ |
| 0.325 | $1.595 + i7.000\cdot10^{-3}$ | $1.814 + i1.377\cdot10^{-1}$ | $1.522 + i1.310\cdot10^{-3}$ | $1.530 + i6.470\cdot10^{-3}$ | $3.389\cdot10^{+1}$ |
| 0.350 | $1.590 + i5.800\cdot10^{-3}$ | $1.988 + i2.175\cdot10^{-1}$ | $1.515 + i1.247\cdot10^{-3}$ | $1.528 + i6.202\cdot10^{-3}$ | $3.405\cdot10^{+1}$ |
| 0.375 | $1.585 + i4.600\cdot10^{-3}$ | $2.187 + i2.708\cdot10^{-1}$ | $1.511 + i1.167\cdot10^{-3}$ | $1.529 + i5.973\cdot10^{-3}$ | $3.473\cdot10^{+1}$ |
| 0.400 | $1.580 + i3.600\cdot10^{-3}$ | $2.396 + i3.004\cdot10^{-1}$ | $1.508 + i1.074\cdot10^{-3}$ | $1.532 + i5.731\cdot10^{-3}$ | $3.575\cdot10^{+1}$ |
| 0.425 | $1.576 + i2.900\cdot10^{-3}$ | $2.601 + i3.091\cdot10^{-1}$ | $1.506 + i9.705\cdot10^{-4}$ | $1.535 + i5.430\cdot10^{-3}$ | $3.691\cdot10^{+1}$ |
| 0.450 | $1.572 + i2.400\cdot10^{-3}$ | $2.786 + i2.995\cdot10^{-1}$ | $1.505 + i8.607\cdot10^{-4}$ | $1.539 + i5.037\cdot10^{-3}$ | $3.802\cdot10^{+1}$ |
| 0.475 | $1.568 + i2.000\cdot10^{-3}$ | $2.936 + i2.744\cdot10^{-1}$ | $1.504 + i7.481\cdot10^{-4}$ | $1.542 + i4.534\cdot10^{-3}$ | $3.889\cdot10^{+1}$ |
| 0.500 | $1.564 + i1.800\cdot10^{-3}$ | $3.036 + i2.366\cdot10^{-1}$ | $1.503 + i6.362\cdot10^{-4}$ | $1.544 + i3.924\cdot10^{-3}$ | $3.933\cdot10^{+1}$ |
| 0.525 | $1.561 + i1.600\cdot10^{-3}$ | $3.071 + i1.888\cdot10^{-1}$ | $1.502 + i5.286\cdot10^{-4}$ | $1.544 + i3.238\cdot10^{-3}$ | $3.916\cdot10^{+1}$ |
| 0.550 | $1.558 + i1.400\cdot10^{-3}$ | $3.041 + i1.369\cdot10^{-1}$ | $1.501 + i4.330\cdot10^{-4}$ | $1.542 + i2.550\cdot10^{-3}$ | $3.817\cdot10^{+1}$ |
| 0.575 | $1.555 + i1.200\cdot10^{-3}$ | $2.978 + i9.386\cdot10^{-2}$ | $1.499 + i3.660\cdot10^{-4}$ | $1.539 + i1.989\cdot10^{-3}$ | $3.619\cdot10^{+1}$ |
| 0.600 | $1.553 + i1.100\cdot10^{-3}$ | $2.917 + i7.320\cdot10^{-2}$ | $1.498 + i3.450\cdot10^{-4}$ | $1.536 + i1.645\cdot10^{-3}$ | $3.304\cdot10^{+1}$ |
| 0.625 | $1.551 + i9.000\cdot10^{-4}$ | $2.877 + i7.711\cdot10^{-2}$ | $1.496 + i3.694\cdot10^{-4}$ | $1.533 + i1.480\cdot10^{-3}$ | $2.898\cdot10^{+1}$ |
| 0.650 | $1.550 + i8.000\cdot10^{-4}$ | $2.849 + i9.299\cdot10^{-2}$ | $1.495 + i4.149\cdot10^{-4}$ | $1.531 + i1.385\cdot10^{-3}$ | $2.488\cdot10^{+1}$ |
| 0.675 | $1.548 + i7.000\cdot10^{-4}$ | $2.828 + i1.078\cdot10^{-1}$ | $1.494 + i4.569\cdot10^{-4}$ | $1.530 + i1.312\cdot10^{-3}$ | $2.158\cdot10^{+1}$ |
| 0.700 | $1.544 + i7.000\cdot10^{-4}$ | $2.808 + i1.163\cdot10^{-1}$ | $1.493 + i4.857\cdot10^{-4}$ | $1.528 + i1.257\cdot10^{-3}$ | $1.936\cdot10^{+1}$ |
| 0.800 | $1.540 + i8.000\cdot10^{-4}$ | $2.744 + i1.073\cdot10^{-1}$ | $1.492 + i5.125\cdot10^{-4}$ | $1.526 + i1.195\cdot10^{-3}$ | $1.716\cdot10^{+1}$ |
| 0.900 | $1.535 + i1.000\cdot10^{-3}$ | $2.704 + i7.996\cdot10^{-2}$ | $1.492 + i5.086\cdot10^{-4}$ | $1.524 + i1.115\cdot10^{-3}$ | $1.587\cdot10^{+1}$ |
| 1.000 | $1.530 + i2.000\cdot10^{-3}$ | $2.683 + i1.016\cdot10^{-1}$ | $1.491 + i6.218\cdot10^{-4}$ | $1.520 + i7.008\cdot10^{-4}$ | $2.392\cdot10^{+0}$ |
| 1.250 | $1.520 + i3.000\cdot10^{-3}$ | | | | |
| 1.500 | $1.510 + i5.000\cdot10^{-3}$ | | | | |
| 2.000 | $1.500 + i8.000\cdot10^{-3}$ | | | | |
| 2.507 | $1.468 + i9.856\cdot10^{-3}$ | | | | |
| 2.614 | $1.475 + i1.139\cdot10^{-2}$ | | | | |
| 2.829 | $1.481 + i4.194\cdot10^{-2}$ | | | | |
| 2.957 | $1.481 + i4.194\cdot10^{-2}$ | | | | |
| 3.043 | $1.481 + i2.920\cdot10^{-2}$ | | | | |
| 3.257 | $1.519 + i1.759\cdot10^{-2}$ | | | | |
| 3.471 | $1.475 + i1.317\cdot10^{-2}$ | | | | |
| 3.686 | $1.481 + i1.075\cdot10^{-2}$ | | | | |
| 3.900 | $1.481 + i6.383\cdot10^{-3}$ | | | | |
| 4.114 | $1.481 + i4.444\cdot10^{-3}$ | | | | |

**Table B2.** Bounds in diameter ($d_A$, $d_B$) of the five size bins of ModelE2.1, with the clay bin split into four sub-bins to allow more accurate calculation of the dust-radiation interaction at ultraviolet and visible wavelengths. The effective diameter ($d_{eff}$) for each bin is also reported.

| Bin | $(d_A, d_B)\,[\mu m]$ | $d_{eff}\,[\mu m]$ |
|---|---|---|
| Clay | (0.1, 0.2) | 0.139 |
| | (0.2, 0.5) | 0.305 |
| | (0.5, 1.0) | 0.693 |
| | (1.0, 2.0) | 1.386 |
| Silt-1 | (2.0, 4.0) | 2.773 |
| Silt-2 | (4.0, 8.0) | 5.546 |
| Silt-3 | (8.0, 16.0) | 11.09 |
| Silt-4 | (16.0, 32.0) | 22.18 |

735 mixture and static accretion (EXT), or spatially and temporally varying for dynamic accretion (INT), we pick intensive optical properties (extinction and scattering efficiency, asymmetry parameter) from an external look-up table that we pre-calculate using a grid of RRIs and IRIs specifically selected to cover typical dust values with high resolution (Table B3). The look-up intensive properties are already integrated over the eight size bins of ModelE2.1 (Table B2), for the sub-set of twenty default shortwave wavelengths, through the same procedure described in Appendix B2. We then derive the optical properties for the

740 actual CRI through bilinear interpolation of the look-up properties corresponding to the four closest grid CRIs. Finally, we average the single-wavelength optical properties over the UV-VIS band of ModelE2.1 following the same method used for default dust (Appendix B2).

**Table B3.** Grid of real ($n_{grd}$) and imaginary ($k_{grd}$) refractive indices included in the external look-up table of single-wavelength size-integrated intensive optical properties (extinction and scattering efficiency, asymmetry parameter), used for the calculation of optical properties for mineral components.

| $n_{grd}$ |
|---|
| $1.490 - 1.500 - 1.510 - 1.520 - 1.530 - 1.540 - 1.550 - 1.560$ |
| $1.570 - 1.580 - 1.590 - 1.600 - 2.000 - 2.400 - 2.800 - 3.200$ |

| $k_{grd}$ |
|---|
| $0 - 0.0001 - 0.0002 - 0.0003 - 0.0004 - 0.0005 - 0.0006 - 0.0007 - 0.0008 - 0.0009$ |
| $0.001 - 0.002 - 0.003 - 0.004 - 0.005 - 0.006 - 0.007 - 0.008 - 0.009$ |
| $0.01 - 0.02 - 0.03 - 0.04 - 0.05 - 0.06 - 0.07 - 0.08 - 0.09$ |
| $0.1 - 0.2 - 0.3 - 0.4 - 0.5 - 0.6 - 0.7 - 0.8 - 0.9 - 1 - 1.1 - 1.2 - 1.3$ |

*Competing interests.* I declare the following competing interests: At least one of the co-authors is a member of the editorial board of Atmospheric Chemistry and Physics.

745 *Acknowledgements.* V. Obiso's effort was supported by the NASA Postdoctoral Program at the NASA Goddard Institute for Space Studies, administered by Oak Ridge Associated Universities under contract with NASA. Additional support was provided by the NASA Modeling, Analysis and Prediction Program (NNG14HH42I) and the Earth Surface Mineral Dust Source Investigation (EMIT), a NASA Earth Ventures Instrument (EVI-4) Mission. Computational resources supporting this work were provided by the NASA High-End Computing (HEC) Program through the NASA Center for Climate Simulation (NCCS) at Goddard Space Flight Center.

750     C. Pérez García-Pando and M. Gonçalves acknowledge funding by the European Research Council under the Horizon 2020 research and innovation programme through the ERC Consolidator Grant FRAGMENT (grant agreement No. 773051), the AXA Research Fund through the AXA Chair on Sand and Dust Storms at BSC, and the European Union's Horizon 2020 research and innovation programme under grant agreement No 821205 (FORCeS).

    The laboratory experiments to retrieve the dust refractive indices in Di Biagio et al. (2017) and Di Biagio et al. (2019) that feed this
755 work received funding from the European Union's Horizon 2020 research and innovation program through the EUROCHAMP–2020 Infrastructure Activity under grant agreement no. 730997. They were supported by the French national programme LEFE/INSU (Les Enveloppes Fluides et l'Environnement/Institut National des Sciences de l'Univers) and by the OSU–EFLUVE (Observatoire des Sciences de l'Univers–Enveloppes Fluides de la Ville à l'Exobiologie) through dedicated research funding to the RED-DUST project. The authors acknowledge the CNRS–INSU for supporting the CESAM chamber as national facility as part of the French ACTRIS Research Infrastructure
760 as well as the AERIS datacenter (www.aeris–data.fr) for distributing and curing the data produced by the CESAM chamber through the hosting of the EUROCHAMP datacenter (https://data.eurochamp.org). C. D. B. was supported by the Centre National des Etudes Spatiales (CNES) and by the CNRS via the Labex L–IPSL, which is funded by the ANR (grant no. ANR–10–LABX–0018).

# References

Adebiyi, A. A. and Kok, J. F.: Climate models miss most of the coarse dust in the atmosphere, Sci. Adv., 6, eaaz9507, 2020.

765 Ahn, H.-J., Park, S.-U., and Chang, L.-S.: Effect of direct radiative forcing of Asian dust on the meteorological fields in East Asia during an Asian dust event period, J. Appl. Meteorol. Climatol., 46, 1655–1681, 2007.

Balkanski, Y., Schulz, M., Claquin, T., and Guibert, S.: Reevaluation of mineral aerosol radiative forcings suggests a better agreement with satellite and AERONET data, Atmos. Chem. Phys., 7, 81–95, 2007.

Bauer, S. E., Tsigaridis, K., Faluvegi, G., Kelley, M., Lo, K. K., Miller, R. L., Nazarenko, L., Schmidt, G. A., and Wu, J.: Historical (1850-770 2014) aerosol evolution and role on climate forcing using the GISS ModelE2.1 contribution to CMIP6, J. Adv. Model. Earth Syst., 12, e2019MS001 978, 2020.

Bedidi, A. and Cervelle, B.: Light scattering by spherical particles with hematite and goethitelike optical properties: Effect of water impregnation, J. Geophys. Res., 98, 11 941–11 952, 1993.

Cakmur, R. V., Miller, R. L., Perlwitz, J., Geogdzhayev, I. V., Ginoux, P., Koch, D., Kohfeld, K. E., Tegen, I., and Zender, C. S.: Constraining 775 the magnitude of the global dust cycle by minimizing the difference between a model and observations, J. Geophys. Res., 111, D06 207, 2006.

Claquin, T., Schulz, M., and Balkanski, Y. J.: Modeling the mineralogy of atmospheric dust sources, J. Geophys. Res., 104, 22 243–22 256, 1999.

Colarco, P. R., Nowottnick, E. P., Randles, C. A., Yi, B., Yang, P., Kim, K.-M., Smith, J. A., and Bardeen, C. G.: Impact of radiatively 780 interactive dust aerosols in the NASA GEOS-5 climate model: Sensitivity to dust particle shape and refractive index, J. Geophys. Res. Atmos., 119, 753–786, 2014.

Derimian, Y., Karnieli, A., Kaufman, Y. J., Andreae, M. O., Andreae, T. W., Dubovik, O., Maenhaut, W., and Koren, I.: The role of iron and black carbon in aerosol light absorption, Atmos. Chem. Phys., 8, 3623–3637, 2008.

Di Biagio, C., Formenti, P., Balkanski, Y., Caponi, L., Cazaunau, M., Pangui, E., Journet, E., Nowak, S., Caquineau, S., Andreae, M. O., 785 Kandler, K., Saeed, T., Piketh, S., Seibert, D., Williams, E., and Doussin, J.-F.: Global scale variability of the mineral dust long-wave refractive index: a new dataset of in situ measurements for climate modeling and remote sensing, Atmos. Chem. Phys., 17, 1901–1929, 2017.

Di Biagio, C., Formenti, P., Balkanski, Y., Caponi, L., Cazaunau, M., Pangui, E., Journet, E., Nowak, S., Andreae, M. O., Kandler, K., Saeed, T., Piketh, S., Seibert, D., Williams, E., and Doussin, J.-F.: Complex refractive indices and single-scattering albedo of global dust aerosols 790 in the shortwave spectrum and relationship to size and iron content, Atmos. Chem. Phys., 19, 15 503–15 531, 2019.

Di Biagio, C., Balkanski, Y., Albani, S., Boucher, O., and Formenti, P.: Direct radiative effect by mineral dust aerosols constrained by new microphysical and spectral optical data, Geophys. Res. Lett., 47, e2019GL086 186, 2020.

Dubovik, O., Holben, B., Eck, T. F., Smirnov, A., Kaufman, Y. J., King, M. D., Tanré, D., and Slutsker, I.: Variability of absorption and optical properties of key aerosol types observed in worldwide locations, J. Atmos. Sci., 59, 590–608, 2002.

795 Formenti, P., Rajot, J. L., Desboeufs, K., Caquineau, S., Chevaillier, S., Nava, S., Gaudichet, A., Journet, E., Triquet, S., Alfaro, S., Chiari, M., Haywood, J., Coe, H., and Highwood, E.: Regional variability of the composition of mineral dust from western Africa: Results from the AMMA SOP0/DABEX and DODO field campaigns, J. Geophys. Res., 113, D00C13, 2008.

Ginoux, P., Chin, M., Tegen, I., Prospero, J. M., Holben, B., Dubovik, O., and Lin, S. J.: Sources and distributions of aerosols simulated with the GOCART model, J. Geophys. Res. Atmos., 106, 20 255–20 273, 2001.

800   Ginoux, P., Garbuzov, D., and Hsu, N. C.: Identification of anthropogenic and natural dust sources using Moderate Resolution Imaging
        Spectroradiometer (MODIS) Deep Blue level 2 data, J. Geophys. Res., 115, D05 204, 2010.

      Go, S., Lyapustin, A., Schuster, G. L., Choi, M., Ginoux, P., Chin, M., Kalashnikova, O., Dubovik, O., Kim, J., da Silva, A., Holben, B., and
        Reid, J. S.: Inferring iron-oxide species content in atmospheric mineral dust from DSCOVR EPIC observations., Atmos. Chem. Phys., 22,
        1395–1423, 2022.

805   Gonçalves Ageitos, M., Obiso, V., Miller, R., Dawson, M., Jorba, O., Klose, M., Balkanski, Y., Perlwitz, J., Basart, S., Di Tomaso, E.,
        Escribano, J., Journet, E., Macchia, F., Montané, G., and Pérez García-Pando, C.: Modeling dust mineralogical composition: sensitivity to
        soil mineralogy atlases and their expected climate impacts, Atmos. Chem. Phys. Discuss., submitted, 2023.

      Green, R. O., Mahowald, N., Ung, C., Thompson, D. R., Bator, L., Bennet, M., Bernas, M., Blackway, N., Bradley, C., Cha, J., Clark,
        P., Clark, R., Cloud, D., Diaz, E., Ben-Dor, E., Duren, R., Eastwood, M. L., Ehlmann, B. L., Fuentes, L., Ginoux, P., Groß, J., He, Y.,
810     Kalashnikova, O., Kert, W., Keymeulen, D., Klimesh, M., Ku, D., Kwong-Fu, H., Liggett, E., Li, L., Lundeen, S., Makowski, M. D.,
        Mazer, A. S., Miller, R., Mouroulis, P., Oaida, B., Okin, G. S., Ortega, A., Oyake, A., Nguyen, H., Pace, T., Painter, T. H., Pempejian, J.,
        Pérez García-Pando, C., Pham, T., Phillips, B., Pollock, R., Purcell, R., Realmuto, V., Schoolcraft, J., Sen, A., Shin, S., Shaw, L., Soriano,
        M., Swayze, G., Thingvold, E., Vaid, A., and Zan, J.: The Earth Surface Mineral Dust Source Investigation: An Earth Science Imaging
        Spectroscopy Mission, in: 2020 IEEE Aerospace Conference, pp. 1–15, 2020.

815   Hand, V. L., Capes, G., Vaughan, D. J., Formenti, P., Haywood, J. M., and Coe, H.: Evidence of internal mixing of African dust and biomass
        burning particles by individual particle analysis using electron beam techniques, J. Geophys. Res., 115, D13 301, 2010.

      Hansen, J. E. and Travis, L. D.: Light scattering in planetary atmospheres, Space Sci. Rev., 16, 527–610, 1974.

      Heinold, B., Helmert, J., Hellmuth, O., Wolke, R., Ansmann, A., Marticorena, B., Laurent, B., and Tegen, I.: Regional modeling of Saharan
        dust events using LM-MUSCAT: Model description and case studies, J. Geophys. Res., 112, D11 204, 2007.

820   Hess, M., Koepke, P., and Schult, I.: Optical Properties of Aerosols and Clouds: The Software Package OPAC, Bull. Am. Meteorol. Soc., 79,
        831–844, 1998.

      Holben, B., Eck, T., Slutsker, I., Tanre, D., Buis, J., Setzer, A., Vermote, E., Reagan, J., Kaufman, Y., Nakajima, T., Lavenu, F., Jankowiak,
        I., and Smirnov, A.: AERONET - a federated instrument network and data archive for aerosol characterization, Remote Sens. Environ.,
        66, 1–16, 1998.

825   Holben, B. N., Eck, T. F., Slutsker, I., Smirnov, A., Sinyuk, A., Schafer, J., Giles, D., and Dubovik, O.: AERONET's Version 2.0 quality
        assurance criteria, Proc. SPIE, Remote Sensing of the Atmosphere and Clouds, 6408, 64 080Q, 2006.

      Huang, Y., Kok, J. F., Kandler, K., Lindqvist, H., Nousiainen, T., Sakai, T., Adebiyi, A., and Jokinen, O.: Climate models and remote sensing
        retrievals neglect substantial desert dust asphericity, Geophys. Res. Lett., 47, e2019GL086 592, 2020.

      Huang, Y., Kok, J. F., Saito, M., and Muñoz, O.: Single-scattering properties of ellipsoidal dust aerosols constrained by measured dust shape
830     distributions, Atmos. Chem. Phys. Discuss., in review, 2023.

      Journet, E., Balkanski, Y., and Harrison, S. P.: A new data set of soil mineralogy for dust-cycle modeling, Atmos. Chem. Phys., 14, 3801–
        3816, 2014.

      Kalashnikova, O. V. and Sokolik, I. N.: Modeling the radiative properties of nonspherical soil-derived mineral aerosols, J. Quant. Spectrosc.
        Radiat. Transf., 87, 137–166, 2004.

835   Kandler, K., Schütz, L., Deutscher, C., Ebert, M., Hofmann, H., Jäckel, S., Jaenicke, R., Knippertz, P., Lieke, K., Massling, A., Petzold,
        A., Schladitz, A., Weinzierl, B., Wiedensohler, A., Zorn, S., and Weinbruch, S.: Size distribution, mass concentration, chemical and

mineralogical composition and derived optical parameters of the boundary layer aerosol at Tinfou, Morocco, during SAMUM 2006, Tellus B: Chem. Phys. Meteorol., 61, 32–50, 2009.

Kelley, M., Schmidt, G. A., Nazarenko, L., Bauer, S. E., Ruedy, R., Russell, G. L., Ackerman, A. S., Aleinov, I., Bauer, M., Bleck, R., Canuto,
840    V., Cesana, G., Cheng, Y., Clune, T. L., Cook, B. I., Cruz, C. A., Del Genio, A. D., Elsaesser, G. S., Faluvegi, G., Kiang, N. Y., Kim, D., Lacis, A. A., Leboissetier, A., LeGrande, A. N., Lo, K. K., Marshall, J., Matthews, E. E., McDermid, S., Mezuman, K., Miller, R. L., Murray, L. T., Oinas, V., Orbe, C., Pérez García-Pando, C., Perlwitz, J. P., Puma, M. J., Rind, D., Romanou, A., Shindell, D. T., Sun, S., Tausnev, N., Tsigaridis, K., Tselioudis, G., Weng, E., Wu, J., and Yao, M.-S.: GISS-E2.1: Configurations and Climatology, J. Adv. Model. Earth Syst., 12, e2019MS002 025, 2020.

845    Kirchstetter, T. W., Novakov, T., and Hobbs, P. V.: Evidence that the spectral dependence of light absorption by aerosols is affected by organic carbon, J. Geophys. Res., 109, D21 208, 2004.

Klose, M., Jorba, O., Gonçalves Ageitos, M., Escribano, J., Dawson, M. L., Obiso, V., Di Tomaso, E., Basart, S., Montané Pinto, G., Macchia, F., Ginoux, P., Guerschman, J., Prigent, C., Huang, Y., Kok, J. F., Miller, R. L., and Pérez García-Pando, C.: Mineral dust cycle in the Multiscale Online Nonhydrostatic AtmospheRe CHemistry model (MONARCH) Version 2.0, Geosci. Model Dev., 14, 6403–6444, 2021.

850    Koch, D., Jacob, D., Tegen, I., Rind, D., and Chin, M.: Tropospheric sulfur simulation and sulfate direct radiative forcing in the Goddard Institute for Space Studies general circulation model, J. Geophys. Res. Atmos., 104, 23 799–23 822, 1999.

Kok, J. F.: A scaling theory for the size distribution of emitted dust aerosols suggests climate models underestimate the size of the global dust cycle, Proc. Natl. Acad. Sci., 108, 1016–1021, 2011.

Kok, J. F., Ridley, D. A., Zhou, Q., Miller, R. L., Zhao, C., Heald, C. L., Ward, D. S., Albani, S., and Haustein, K.: Smaller desert dust cooling
855    effect estimated from analysis of dust size and abundance, Nat. Geosci., 10, 274–278, 2017.

Kok, J. F., Adebiyi, A. A., Albani, S., Balkanski, Y., Checa-Garcia, R., Chin, M., Colarco, P. R., Hamilton, D. S., Huang, Y., Ito, A., Klose, M., Leung, D. M., Li, L., Mahowald, N. M., Miller, R. L., Obiso, V., Pérez García-Pando, C., Rocha-Lima, A., Wan, J. S., and Whicker, C. A.: Improved representation of the global dust cycle using observational constraints on dust properties and abundance, Atmos. Chem. Phys., 21, 8127–8167, 2021.

860    Li, J., Carlson, B. E., Dubovik, O., and A., L. A.: Recent trends in aerosol optical properties derived from AERONET measurements, Atmos. Chem. Phys., 14, 12 271–12 289, 2014.

Li, L., Mahowald, N. M., Miller, R. L., Pérez García-Pando, C., Klose, M., Hamilton, D. S., Gonçalves Ageitos, M., Ginoux, P., Balkanski, Y., Green, R. O., Kalashnikova, O., Kok, J. F., Obiso, V., Paynter, D., and Thompson, D. R.: Quantifying the range of the dust direct radiative effect due to source mineralogy uncertainty, Atmos. Chem. Phys., 21, 3973–4005, 2021.

865    Longtin, D. R., Shettle, E. P., Hummel, J. R., and Pryce, J. D.: A wind dependent desert aerosol model: radiative properties, Tech. Rep. Technical Report AFGL-TR-88-0112, Air Force Geophysics Laboratory, Hanscom AFB, MA, 1988.

Markel, V. A.: Introduction to the Maxwell Garnett approximation: tutorial, J. Opt. Soc. Am. A, 33, 1244–1256, 2016.

Meng, Z., Yang, P., Kattawar, G. W., Bi, L., Liou, K. N., and Laszlo, I.: Single-scattering properties of tri-axial ellipsoidal mineral dust aerosols: A database for application to radiative transfer calculations, J. Aerosol Sci., 41, 501–512, 2010.

870    Miller, R. L., Tegen, I., and Perlwitz, J.: Surface radiative forcing by soil dust aerosols and the hydrologic cycle, J. Geophys. Res. Atmos., 109, D04 203, 2004.

Miller, R. L., Cakmur, R. V., Perlwitz, J., Geogdzhayev, I. V., Ginoux, P., Koch, D., Kohfeld, K. E., Prigent, C., Ruedy, R., Schmidt, G. A., and Tegen, I.: Mineral dust aerosols in the NASA Goddard Institute for Space Sciences ModelE atmospheric general circulation model, J. Geophys. Res., 111, D06 208, 2006.

875   Miller, R. L., Knippertz, P., Pérez García-Pando, C., Perlwitz, J. P., and Tegen, I.: Impact of Dust Radiative Forcing upon Climate, in: Mineral
        Dust: a Key Player in the Earth System, edited by Knippertz, P. and Stuut, J.-B. W., chap. 13, pp. 327–357, Springer, 2014.

Miller, R. L., Schmidt, G. A., Nazarenko, L., Bauer, S. E., Kelley, M., Ruedy, R., Russell, G. L., Ackerman, A., Aleinov, I., Bauer, M., Bleck,
        R., Canuto, V., Cesana, G., Cheng, Y., Clune, T. L., Cook, B., Cruz, C. A., Del Genio, A. D., Elsaesser, G. S., Faluvegi, G., Kiang, N. Y.,
        Kim, D., Lacis, A. A., Leboissetier, A., LeGrande, A. N., Lo, K. K., Marshall, J., Matthews, E. E., McDermid, S., Mezuman, K., Murray,
880   L. T., Oinas, V., Orbe, C., Pérez García-Pando, C., Perlwitz, J. P., Puma, M. J., Rind, D., Romanou, A., Shindell, D. T., Sun, S., Tausnev,
        N., Tsigaridis, K., Tselioudis, G., Weng, E., Wu, J., and Yao, M.-S.: CMIP6 historical simulations (1850-2014) with GISS-E2.1, J. Adv.
        Model. Earth Syst., 13, e2019MS002 034, 2021.

Mishchenko, M. I., Travis, L. D., and Lacis, A. A.: Scattering, Absorption and Emission of Light by Small Particles, Cambridge University
        Press, 2002.

885   Moosmüller, H., Engelbrecht, J. P., Skiba, M., Frey, G., Chakrabarty, R. K., and Arnott, W. P.: Single scattering albedo of fine mineral dust
        aerosols controlled by iron concentration, J. Geophys. Res., 117, D11 210, 2012.

Panta, A., Kandler, K., Alastuey, A., González-Flórez, C., González-Romero, A., Klose, M., Querol, X., Reche, C., Yus-Díez, J., and Pérez
        García-Pando, C.: Insights into the single particle composition, size, mixing state and aspect ratio of freshly emitted mineral dust from
        field measurements in the Moroccan Sahara using electron microscopy, Atmos. Chem. Phys. Discuss., in review, 2022.

890   Patterson, E. M., Gillette, D. A., and Stockton, B. H.: Complex index of refraction between 300 and 700 nm for Saharan aerosols, J. Geophys.
        Res., 82, 3153–3160, 1977.

Pausata, F. S. R., Messori, G., and Zhang, Q.: Impacts of dust reduction on the northward expansion of the African monsoon during the
        Green Sahara period, Earth Planet. Sci. Lett., 434, 298–307, 2016.

Pérez, C., Nickovic, S., Pejanovic, G., Baldasano, J. M., and Özsoy, E.: Interactive dust-radiation modeling: A step to improve weather
895     forecasts, J. Geophys. Res., 111, D16 206, 2006.

Pérez García-Pando, C., Miller, R. L., Perlwitz, J. P., Rodríguez, S., and Prospero, J. M.: Predicting the mineral composition of dust aerosols:
        Insights from elemental composition measured at the Izaña Observatory, Geophys. Res. Lett., 43, 10 520–10 529, 2016.

Perlwitz, J. P., Pérez García-Pando, C., and Miller, R. L.: Predicting the mineral composition of dust aerosols –Part 1: representing key
        processes, Atmos. Chem. Phys., 15, 11 593–11 627, 2015a.

900   Perlwitz, J. P., Pérez García-Pando, C., and Miller, R. L.: Predicting the mineral composition of dust aerosols –Part 2: Model evaluation and
        identification of key processes with observations, Atmos. Chem. Phys., 15, 11 629–11 652, 2015b.

Querry, M. R.: Optical Constants, Tech. Rep. Contractor Report CRDC-CR-85034, University of Missouri, Kansas City, MO, 1985.

Ridley, D. A., Heald, C. L., Kok, J. F., and Zhao, C.: An observationally-constrained estimate of global dust aerosol optical depth, Atmos.
        Chem. Phys., 16, 15 097–15 117, 2016.

905   Ryder, C. L., Highwood, E. J., Lai, T. M., Sodemann, H., and Marsham, J. H.: Impact of atmospheric transport on the evolution of micro-
        physical and optical properties of Saharan dust, Geophys. Res. Lett., 40, 2433–2438, 2013a.

Ryder, C. L., Highwood, E. J., Rosenberg, P. D., Trembath, J., Brooke, J. K., and Bart, J. K.: Optical properties of Saharan dust aerosol and
        contribution from the coarse mode as measured during the Fennec 2011 aircraft campaign, Atmos. Chem. Phys., 13, 303–325, 2013b.

Samset, B. H., Stjern, C. W., Andrews, E., Kahn, R. A., Myhre, G., Schulz, M., and Schuster, G. L.: Aerosol Absorption: Progress Towards
910     Global and Regional Constraints, Curr. Clim. Change Rep., 4, 65–83, 2018.

Scanza, R. A., Mahowald, N., Ghan, S., Zender, C. S., Kok, J. F., Liu, X., Zhang, Y., and Albani, S.: Modeling dust as component minerals in the Community Atmosphere Model: development of framework and impact on radiative forcing, Atmos. Chem. Phys., 15, 537–561, 2015.

Scheuvens, D. and Kandler, K.: On Composition, Morphology, and Size Distribution of Airborne Mineral Dust, in: Mineral Dust: A Key Player in the Earth System, edited by Knippertz, P. and Stuut, J.-B. W., chap. 2, pp. 15–49, Springer, 2014.

Schmidt, G. A., Kelley, M., Nazarenko, L., Ruedy, R., Russell, G. L., Aleinov, I., Bauer, M., Bauer, S. E., Bhat, M. K., Bleck, R., Canuto, V., Chen, Y.-H., Cheng, Y., Clune, T. L., Del Genio, A., de Fainchtein, R., Faluvegi, G., Hansen, J. E., Healy, R. J., Kiang, N. Y., Koch, D., Lacis, A. A., LeGrande, A. N., Lerner, J., Lo, K. K., Matthews, E. E., Menon, S., Miller, R. L., Oinas, V., Oloso, A. O., Perlwitz, J. P., Puma, M. J., Putman, W. M., Rind, D., Romanou, A., Sato, M., Shindell, D. T., Sun, S., Syed, R. A., Tausnev, N., Tsigaridis, K., Unger, N., Voulgarakis, A., Yao, M.-S., and Zhang, J.: Configuration and assessment of the GISS ModelE2 contributions to the CMIP5 archive, J. Adv. Model. Earth Syst., 6, 141–184, 2014.

Schuster, G. L., Dubovik, O., and Arola, A.: Remote sensing of soot carbon - Part 1: distinguishing different absorbing aerosol species, Atmos. Chem. Phys., 16, 1565–1585, 2016.

Sinyuk, A., Torres, O., and Dubovik, O.: Combined use of satellite and surface observations to infer the imaginary part of refractive index of Saharan dust, Geophys. Res. Lett., 30, 1081, 2003.

Sinyuk, A., Holben, B. N., Eck, T. F., Giles, D. M., Slutsker, I., Korkin, S., Schafer, J. S., Smirnov, A., Sorokin, M., and Lyapustin, A.: The AERONET Version 3 aerosol retrieval algorithm, associated uncertainties and comparisons to Version 2, Atmos. Meas. Tech., 13, 3375–3411, 2020.

Sokolik, I. N. and Toon, O. B.: Incorporation of mineralogical composition into models of the radiative properties of mineral aerosol from UV to IR wavelengths, J. Geophys. Res., 104, 9423–9444, 1999.

Strong, J. D. O., Vecchi, G. A., and Ginoux, P.: The response of the tropical Atlantic and West African climate to Saharan dust in a fully coupled GCM, J. Clim., 28, 7071–7092, 2015.

Tegen, I. and Fung, I.: Modeling of mineral dust in the atmosphere: Sources, transport, and optical thickness, J. Geophys. Res., 99, 22 897–22 914, 1994.

Thekaekara, M. P.: Solar Energy Monitor in Space (SEMIS), Tech. Rep. NASA-TM-X-70623, X-912-74-78, NASA Goddard Space Flight Center, Greenbelt MD, 1974.

van der Does, M., Korte, L. F., Munday, C. I., Brummer, G.-J. A., and Stuut, J.-B. W.: Particle size traces modern Saharan dust transport and deposition across the equatorial North Atlantic, Atmos. Chem. Phys., 16, 13 697–13 710, 2016.

Volz, F. E.: Infrared optical constants of ammonium sulfate, Sahara dust, volcanic pumice and flyash, Appl. Opt., 12, 564–568, 1973.

Yoshioka, M., Mahowald, N. M., Conley, A. J., Collins, W. D., Fillmore, D. W., Zender, C. S., and Coleman, D. B.: Impact of Desert Dust Radiative Forcing on Sahel Precipitation: Relative Importance of Dust Compared to Sea Surface Temperature Variations, Vegetation Changes, and Greenhouse Gas Warming, J. Clim., 20, 1445–1467, 2007.

Zhang, X. L., Wu, G. J., Zhang, C. L., Xu, T. L., and Zhou, Q. Q.: What is the real role of iron oxides in the optical properties of dust aerosols?, Atmos. Chem. Phys., 15, 12 159–12 177, 2015.